Tunable membranes incorporating artificial water channels for high-performance brackish/low-salinity water reverse osmosis desalination

Maria Di Vincenzo, Alberto Tiraferri, Valentina-Elena Musteata, Stefan Chisca, Mihai Deleanu, Francesco Ricceri, Didier Cot, Suzana Nunes, Mihail Barboiu

PNAS
www.pnas.org

Main Manuscript for

Tunable membranes incorporating artificial water channels for high-performance brackish/low salinity water reverse osmosis desalination

Maria Di Vincenzo,[1] Alberto Tiraferri,[2] Valentina-Elena Musteata,[3] Stefan Chisca,[3] Mihai Deleanu,[1] Francesco Ricceri,[2] Didier Cot,[1] Suzana P. Nunes,[3] Mihail Barboiu[*1]

[1]Institut Européen des Membranes, Adaptive Supramolecular Nanosystems Group, University of Montpellier, ENSCM, CNRS, Place Eugène Bataillon, CC 047, F-34095, Montpellier, France.

[2]Department of Environment, Land and Infrastructure Engineering (DIATI), Politecnico di Torino, Corso Duca degli Abruzzi 24, 10129 Turin, Italy.

[3]King Abdullah University of Science and Technology (KAUST), Biological and Environmental Science and Engineering Division, Advanced Membranes and Porous Materials Center, 23955-6900, Thuwal, Saudi Arabia.

*Mihail Barboiu

Email: mihail-dumitru.barboiu@umontpellier.fr

Author Contributions: M.B. designed the research, M.D.V., M.D. and F.R. performed the experiments, V.E.M. and S.C. performed and analyzed TEM data, D.C. performed the SEM data A.T., S.P.N. and M.B. wrote the paper.

Competing Interest Statement: The authors declare the following competing financial interests: the results reported in this paper were filled in provisional patent no FR1910152, sept 2019 by M.D.V., A.T. and M.B.

Classification: Paste the major and minor classification here. Dual classifications are permitted, but cannot be within the same major classification.

Keywords: artificial water channels; self-assembly; bio-inspired membranes; reverse osmosis; desalination

Abstract

Membrane-based technologies have a tremendous role in water purification and desalination. Inspired by biological proteins, artificial water channels (AWC) have been proposed to overcome the permeability/selectivity trade-off of desalination processes. Promising strategies exploiting the AWC with Å-scale selectivity, have revealed their impressive performances when embedded in bilayer membranes. Herein, we demonstrate that self-assembled imidazole-quartet (I-quartet) AWCs are macroscopically incorporated within industrially relevant reverse osmosis membranes. In particular, we explore the best combination between I-quartet AWC and m-phenylenediamine (MPD) monomer to achieve a seamless incorporation of AWC in a defect-free polyamide membrane. The performance of the membranes is evaluated by cross-flow filtration under real reverse osmosis conditions (15-20 bar of applied pressure) by filtration of brackish feed streams. The optimized bio-inspired membranes achieve an unprecedented improvement, resulting in more than twice (up to 6.9 L $m^{-2}h^{-1}$ bar^{-1}) water permeance of analogous commercial membranes, while maintaining excellent NaCl rejection (>99.5%). They show also excellent performance in the purification of low-salinity water under low-pressure conditions (6 bar of applied pressure) with fluxes up to 35 L $m^{-2}h^{-1}$ and 97.5-99.3% observed rejection.

Significance Statement

Inspired by biological models, artificial water channels can be used to overcome the permeability/selectivity trade-off of traditional desalination membranes. We demonstrate that rational incorporation of I–quartet artificial water channels in composite polyamide membranes synthesized *via* interfacial polymerization, provide defect free biomimetic membranes with intrinsic water-to-salt permeability on the operational Brackish water reverse osmosis-BWRO/ Tap water reverse osmosis-TWRO desalination pressure and medium/low salinity conditions.

Introduction

Competition over increasingly contaminated freshwater resources during the last decades has made the availability to safe drinking water a serious global challenge for the 21st century. Desalination is one of the solutions to the problem of freshwater scarcity, along with environmental remediation technologies and sustainable conservation policies.[1,2] Currently, about 100 million m^3/day of desalinated water is being produced, with an annual increase of more than 10 %.Traditional reverse osmosis (RO) membranes are thin-film composites (TFC), which rely on a supported polyamide layer to perform water/solute separations.[3,4]

Synthetic membranes act by dissolving and diffusing solutes with scale selectivity through their polymeric matrix: a material property that leads to a permeability-selectivity trade-off behavior.[5] Numerous approaches have been proposed to overcome this limitation, including membrane grafting, chemical functionalization, and processes optimization.[6-10] Despite several elegant design strategies, membrane-based technologies always report an improved water permeability at the expense of lower selectivity, or vice versa.[11] Although membrane-based separation offers energy efficiency, excellent water quality, and capability for implementation at industrial scale, there is a pressing need for membranes with both improved selectivity and enhanced permeability, especially for increasing the efficiency of the 0 purification technology.[2,4]

Recent advances have made materials prepared under molecular control increasingly more attractive to researchers, offering the possibility of stable and high efficiency bio-inspired membranes.[1,2] Due to their unique functional design, biological aquaporins and artificial water channels (AWC), with proven high performances at the Å-scale, when embedded in lipid bilayers, have inspired their incorporation into desalination membranes.[12,13] Self-assembled[14,15] and unimolecular[16] AWCs have been developed during the last decade with the hope to mimic the complex biological machinery.[17-19] These approaches have shown that AWCs are mostly active when embedded in lipid bilayers, but upscaling methods toward biomimetic RO polymeric membrane that can be prepared at industrial standards is possible.[2]

The defects created at the interface between active AWCs and surrounding matrices are critical for the performances of RO membrane for desalination. When fabricating a high-performance RO membrane for desalination, a number of necessary characteristics need to be achieved to maximize the productivity, including suitable mechanical resistance, high density of the functional channels per unit area and, perhaps the most ambitious of all, the absence of defects.[1] We postulated that one of the creative strategies for addressing the scale-up challenges and improved performances is to combine the established polyamide (PA) material prepared *via* interfacial polymerization (IP) and known for its easy scalability *via* the integration within a typical roll-to-roll processing system, with both permeable and selective AWCs.[2]

We previously reported the fabrication of a biomimetic membranes, containing I-quartet AWCs embedded in a classical polyamide PA.[2] We know that compositional diversity of PA components and additives have a tremendous impact on membrane structure and performances.[1] In the present report, our novel strategy leads to a greater fundamental understanding of how AWC incorporation influence the performance of PA/AWC membranes. The novel reported hybrid AWC-PA materials can be optimized at the nanoscale with different morphologies and chemical properties by the optimal mixing of various recipes exploiting variable amounts of AWCs and PA components. Specifically, we investigate valuable insights into fabrication-structure-performance relationship and discuss the effect of composition of AWC and m-phenylenediamine components for improving and discovering new performances of bioinspired membranes. The novelty here is related to the straightforward quantification of specific compositions, that allow obtainment of seamless active layers in which AWCs are gently and optimally incorporated without creating defects, in all cases. Homogeneous sponge-like superstructures of hybrid PA-AWC materials are thus achieved and applied under new filtration conditions real brackish water and low-salinity-water RO desalination conditions.

Results

Formation pathways of control and bioinspired reverse osmosis membranes. The imidazole-quartet, I-quartet,[14,15] comprises stacks of four molecules **HC6** and two water molecules that form a pore diameter of 2.6 Å filled with oriented single water wires (Fig. 1a).[20] The water orientation[21] is of prime importance for enhancing its translocation in the range of 10^6-10^7 water molecules·s^{-1} per channel, with a perfect salt rejection via a single wire[20] or sponge cluster[17] mechanism. The crystal packing reveals parallel sheets of the alternative I-quartets self-assembled in a lamellar phases of parallel single water channels (Fig. 1c,d) and matching well with the ordered rows observed in the TEM micrograph of a crystalline powder obtained from the evaporation of an ethanolic aqueous casting solution of **HC6** (Fig. 1b).

The RO membranes in this study were prepared by interfacial polymerization (IP) of m-phenylenediamine (MPD) and trimesoylchloride (TMC), resulting in the formation of polyamide (PA) layers onto a commercial polysulfone (PSf) support. For the synthesis of bioinspired PA layers, the conventional IP procedure was preceded by the incorporation of AWCs (Fig. 1e). In a first step, an ethanolic aqueous solution of **HC6** results in the formation of stable colloidal aggregates (D_h = 200 nm), observed by dynamic light scattering DLS when water was added to ethanolic solutions of **HC6**, without any visible precipitation. Please note that compared with other previously studied channels **HC4**-**HC8**, **HC6** with an optimal solubility, avoid precipitation under described IP experimental conditions leading to the formation of free defect membranes. This aqueous solution was poured onto the PSf support which was then immersed in an aqueous MPD solution, resulting in the formation of hybrid AWC/MPD nanosized colloidal aggregates. The DLS analysis shows that smaller aggregates (D_h = 70 nm) (See SI Appendix, Fig. S1) were obtained when an aqueous solution of MPD was used instead of pure water, reminiscent of H-bonding interactions between AWC and MPD.[2] The integration of AWC into PA hybrid layers is firstly related to a nucleation process of such colloidal structures; then, a heterogeneous nucleation is promoted by H-bonding interactions between MPD and colloidal AWC nano-aggregates, as shown by DLS, while any precipitation process was observed. Based on this information, different **HC6**/MPD ratios were investigated to explore the effect of the composition on the material morphology that control and tune the membrane transport performances (See SI Appendix, Table S1). We know that, over the period of incipient formation of the PA film, the polymer growth remains nearly constant, being determined by the diffusion rate of the MPD monomers in the organic phase.[22] An excess of MPD is required to promote a significant diffusion into the organic phase during film formation; therefore, an equal or sub-stoichiometric amount of MPD may result in a lower polymerization degree.[23,24] After the immersion of the support layer into the MPD solution, the excess solution was removed with an air gun from the surface, and the **HC6**-MPD-saturated support was immersed into a TMC solution to form the PA layer. In this step, the AWC/MPD amphiphilic colloidal aggregates might help the migration of the MPD to the organic phase, favoring the IP reaction, while they may synergistically interact with the growing PA segments *via* H-bonding. We surmise that this process results in the formation of cross-linked hybrid AWC-PA materials. Following the IP procedures to prepare both the control and the bioinspired membranes, they were cured in DI water at 95 °C, dipped in a 200 ppm NaOCl aqueous solution, and then in a 1000 ppm $NaHSO_3$ aqueous solution. The membranes were finally rinsed and stored in DI water at 4 °C before testing or characterization.

Morphological / structural properties of the bioinspired membranes. Evidence of AWCs incorporation. Fourier Transform Infrared (FTIR) spectra demonstrate the formation of a hybrid PA-AWC networks (See SI Appendix, Fig. S2 a,b). Vibration bands associated with amide bonds of the PA are visible in all IR spectra, namely, the peaks at 1502 cm^{-1} (amide-II, N–H in-plane bending) and 1666 cm^{-1} (amide-I, C=O stretching vibration).[22] Evidence for AWCs incorporation within hybrid PA membranes was obtained from the vibration shifts at 1585 cm^{-1} and 1609 cm^{-1}, assigned to the C=C stretching of the imidazole and to the C=O stretch of the urea groups, as well as the -$CH_{2,as}$ and -$CH_{2,sym}$ stretch modes of the alkyl chains of **HC6** visible in the range 2750 and 2957 cm^{-1}, respectively. The sharp band centered around 3400 cm^{-1} is attributed to the O-H

stretching vibration of strongly H-bonded water within I-quartet channels. This band became broad for the TFC-**HC6** membrane, due to the presence of more mobile less dense H-bonded water within the matrix of the bioinspired layer. This new type of PA-AWC hybrid material generated *via* a nucleation/IP mechanism, is reminiscent of the emergence of self-assembled I-quartets within a porous sponge-like membrane that theoretically present enhanced water permeation as showed by our previous molecular modeling studies.[17] They are suggestive of dynamic superstructures to provide cooperatively interconnected membrane-spanning pathways through water networks.

Fig. S2b, See SI Appendix, presents the average elemental mass fraction X% obtained from energy dispersive X-ray spectroscopy (EDX) analysis for bioinspired membranes prepared by keeping constant the amount of **HC6** and varying MPD concentration. When compared to the control TFC membranes presenting a C % of 61-67 w % as previously reported in literature for traditional PA membranes,[23,24] the C % of 80-85 w % was significantly higher in all the bioinspired PA-AWC layers. This result is expected because the C/O mass ratio of **HC6** is significantly higher (~10) than that of PA (~3.5-4), thus providing additional evidence of AWCs incorporation in hybrid AWC-PA layers. By reducing the MPD molar ratio, thereby decreasing the density of amine moieties and amide bonds, the N % decreased and the relative C % increased by roughly 4%.

Scanning electronic microscopy (SEM) micrographs (Fig.2 and See SI Appendix, Fig. S3) suggest that the morphology of the layer and the level of **HC6** incorporation can be tuned by adjusting the MPD/**HC6** ratio during membrane fabrication. All the bioinspired layers appeared continuous and free of microscopic defects. The nano- and micro-structures of PA-layers governing mass transport is strongly dependent on the cross-linking degree of PA, influencing the density and distribution of AWCs within the PA matrix. In general, with a constant **HC6** load, as the concentration of MPD was reduced in the fabrication solution, the top surface evolved from a “ridge-and-valley” morphology (an effect of the rapid diffusion of concentrated MPD into the organic phase), typical of conventional PA layers, to a “flake-like” morphology (See SI Appendix, Figs S4, S5) observed for lower MPD concentrations. In addition to a change in the surface roughness, the bioinspired membranes with higher **HC6** loads and medium to high MPD concentrations displayed a distinct, highly porous core structure, with a relatively large thickness ranging from 150 to 300 nm. Even more interestingly, all the layers prepared in the presence of **HC6** further comprised a diffuse distribution of sponge like-packed superstructures that spanned the whole active layer (Fig. 2a,b and See SI Appendix, Fig. S6). These innovative inner nanostructures and overall morphology appeared to be pronounced for the membrane referred to as 0.8-**HC6** (0.8% w/w MPD and the optimal load of 1.5% w/w **HC6**), shown in Fig. 2c,d. Clearly, the cross-section of this representative bioinspired membrane was characterized by: (i) a smoother upper surface compared to the control TFC membrane, (ii) a highly porous multi-layer structure comprising large voids, (iii) a greater overall thickness and (iv) the presence of high-density and homogeneously distributed nanoparticles embedded in the PA matrix. The best combination of productivity and selectivity was obtained with this membrane in experimental brackish water reverse osmosis tests (*vide infra*). When bioinspired PA-AWC layers were instead prepared with a sub-stoichiometric MPD molar ratio (≤ 0.4 % w/w), the concentration of this monomer became the dominant factor governing the final film structure: these layers were generally free of underlying large voids and were characterized by a much smaller average thickness of 50 nm; see the representative samples in Fig. 2e-f. The sponge-like nanostructures embedded in the layer were still observed, although with apparently lower density, possibly due to a more difficult incorporation in thin-films with smaller polymerization degree. This result suggests that the complex core structure of the selective layer embedding self-aggregated AWC-PA sponge-like superstructures is a strong function of both the **HC6**/MPD ratios and the absolute monomer concentrations employed during fabrication, and that the layer architecture can ultimately be controlled by these parameters to tune and improve the RO performance, which is described in detail below.

The surface morphology of the bioinspired PA layers was further investigated by atomic force microscopy-AFM (See SI Appendix, Fig. S7). In agreement with the SEM analysis, revealing the

disappearance of the rough ridge-and-valley features, values of RMS <100 nm roughness were found for membranes fabricated with MPD concentrations below 2% w/w. These RMS values are lower than typical values of 100 - 300 nm often observed for classical PA membranes.[27] The average roughness, indicative of the overall thickness of the layer, increased when the bioinspired membranes were fabricated using 1.5 % w/w **HC6** and 0.8-1.2 % w/w MPD (Fig. 3a-f), in accordance with the greater internal porosity and thickness of the morphologies observed in SEM micrographs.

Transmission electronic microscopy (TEM) cross-sectional images in Fig. 3 also evidence that by increasing the MPD concentration from 0.2 to 2.0% w/w while keeping constant the amount of **HC6** (1.5% w/w) leads to an increase of membrane thickness; the maximum height of the PA layer correlates with the amount of MPD, with alternating thinner / thicker regions on the top of the PSf support. For 0.2 and 0.4 w/w % MPD (Fig. 3a, b), the PA layer has a more irregular aspect, encompassing larger portions (up to 1 μm, as observed in TEM cross-sections of the 0.2-HC6 membrane) with 20 - 40 nm thickness, portions with more regular aspect of ridge and valley and areas with higher thickness (up to 240 nm and 170 nm for 0.2 and respectively, 0.4-HC6). Starting with 0.8-1.8 w/w % MPD, (Fig. 3c-e) the IP layer has a more uniform aspect with ridge and valley morphology. In addition, more developed areas with branches more equally grown in all dimensions (with flower/rose-like morphology) are being observed. For these membranes, the PA layer has a more tortuous appearance and therefore, a higher surface area. It is also clear that the IP layer has a complex internal structure when the AWC are added, with specific nanoparticulate domains present over its whole thickness. AWC/PA nanoparticles, corresponding to the brighter spots and having a diameter of ~15-20 nm in the middle of the PA layer for 0.2 and 0.4 w/w % MPD, while higher density of nanoparticles are observed for 0.8-1.8 w/w % MPD. In addition, they are more equally distributed across the membranes thickness, from the top to the bottom of the layer. These less dense white regions are filled by porous nanoparticles of AWC/PA hybrids during the PA formation. This apparent lower layer density may lead to a lower resistance to transport that would in part explain larger water permeance values observed for the TFC-**HC6** films. In summary, a low concentration of MPD promoted the formation of a smoother surface, while the presence of **HC6** during IP produced thicker and more porous selective layers compared to their reference TFC counterparts free of **HC6**. In addition, appropriate loadings of MPD above 0.4 % w/w and of **HC6** below 1.8% w/w, together with an appropriate ratio of **HC6**/MPD of 0.7-1.9 (w/w) during fabrication, allowed suitable embedding of self-assembled AWC/PA nanoparticles within the PA layer, which are hypothesized to promote faster and selective water passage during membrane filtration.

Performance of the membranes in low-pressure RO filtration of brackish water. The filtration performance of bioinspired membranes was measured in brackish water reverse osmosis (BWRO) and tap water reverse osmosis (TWRO) desalination.[25]

First, the BWRO performances (i.e., water permeance, *A*, and the solute permeability coefficient, *B)* were evaluated for membranes prepared by varying the **HC6** loading from 0 % (control TFC) to 1.8% w/w, while keeping the MPD concentration constant (3.4 % w/w) (Fig. 4a,b). By increasing the **HC6** loading, membranes exhibited progressively higher water permeance increasing from 1.5 to 3.5 L $m^{-2}h^{-1}bar^{-1}$, with up to 185% increase with respect to the control TFC membrane, while maintaining very low and near uniform salt fluxes up to around 1.3% w/w **HC6** of initial loading. Above this concentration, a drop of performance was observed. This result is rationalized with the **HC6** concentration at the highest loading of 1.8 % w/w, which inhibited the formation of a defect-free selective layer during IP, also suggested by the large error bars related to erratic filtration performance of different samples fabricated using the same procedure. This set of filtration results translated into values of *A*/*B* with a peak for concentrations of 0.9 % w/w **HC6**. Then, we observed that by lowering the MPD concentration to 2 % w/w, higher values of water permeances were obtained with an average *A* of 4.5 L $m^{-2}h^{-1}bar^{-1}$ and low salt passage: 99.8 % real NaCl average rejection were observed up to 1.5 % w/w **HC6** loading (empty symbols in Fig. 4 a,b).

We know that the MPD concentration control its diffusion into the organic phase when IP reaction is occurring,[23] but this parameter also interferes with the **HC6** aggregation through H-bonding. Therefore, the **HC6**/MPD ratio clearly determines the final layer morphology and transport properties. With these assumptions in mind, further experiments aimed at investigating lower MPD concentrations, from 2 % to 0.2 % w/w, combined with an optimal **HC6** loading, fixed at 1.5 % w/w (Fig. 4c,d). The best samples prepared with this loading showed a consistent value of *A*/*B* close to ~35 1/bar, thus associated with an overall remarkable permeability-selectivity combination to be applied in BWRO desalination, whereby membranes with a permeance of >3 L $m^{-2}h^{-1}bar^{-1}$ are required. Under BWRO conditions, the water permeance increased significantly and reached a peak of ~6.9 L m^{-2} h^{-1} bar^{-1} for the MPD concentration of 0.8-1.2 % w/w, while maintaining very low associated salt fluxes rates. This result represents an exceptional ~360 % increase in water permeance at equivalent *A*/*B* ratio, with respect to the best membrane fabricated using 3.4% w/w MPD concentration and a ~130% increase in water permeance compared to commercial BW30 membranes (permeance of ~3.0 L m^{-2} $h^{-1}bar^{-1}$ and 99.5 % NaCl rejection), with comparable observed NaCl rejection of ≥99.4%. We noted that the membrane performance dropped rapidly by using sub-stoichiometric MPD concentrations lower than 0.8 % w/w. The data suggest that a maximum loading of **HC6** of 1.8% w/w and minimum loading of MPD of 0.4% w/w are needed to construct the optimal porous sponge-like AWC/PA structures and to prevent the formation of defects in the selective layer. Also, there is a clearly optimal combination of 0.8-1.2% w/w MPD with 1.5% w/w **HC6**, for a resulting **HC6**/MPD ratio of roughly 1.2 w/w to achieve high-performance defect-free bioinspired membranes.

Performance of the membranes in low-pressure RO filtration of Tap water. This study also aimed at evaluating the performances of bioinspired membranes for TWRO desalination. The water flux followed the same trend measured under BWRO desalination, decreasing from 34 to 24 L m^{-2} h^{-1} by increasing the MPD concentration from 0.8% w/w to 1.8% w/w with a constant optimal **HC6** load of 1.5% w/w (applied pressure of 6 bar, Table S5, S6). Simultaneously, the observed rejections based on global conductivity measurements grew accordingly, from 97.5% to 99.3% (Fig. 4e). These values are in the same range, and in some cases slightly higher, of those measured under the same experimental conditions with commercial TWRO membranes (31±1 L m^{-2} h^{-1}; 97.5 % observed rejection), such as the TW30 from DuPont. Furthermore, multivalent cations including Ca^{2+} were rejected at a higher rate of 99.8 % compared to Na^{+} and K^{+} cations, due to size exclusion mechanism,[26] specifically indicating the potential of these membranes for water softening applications (Fig. 4f).

Discussion

Relationship between structural behavior and transport performance of the biomimetic membranes. The present study leads to the discovery of an unexplored mechanistic strategy allowing homogeneous AWC incorporation starting from their in-situ colloidal self-assembled superstructures leading to the identification of sponge-like particles present within the hybrid PA-AWC materials. During IP, the MPD is interacting with soft self-assembled **HC6** colloidal nanoparticles *via* H-bonding. Due to their amphiphilic properties, the AWC aggregates may also contribute to enhance the diffusion of the MPD into the organic phase to react with the TMC as revealed by previous studies.[27] The formation of the hybrid layers may be further generated *via* the interaction of the amphiphilic AWC/MPD nanoparticles with nascent PA oligomers *via* H-bonding. These interactions depend strongly on the **HC6**/MPD ratio and under favorable conditions, they effectively promote the PA formation and facilitate the gentle incorporation of AWC aggregates, whereby preventing the formation of defects, which are commonly observed when solid state nanoparticles are directly incorporated within the PA.[1,2] Other than the seamless *in-situ* adaptive incorporation of distributed AWC/PA-sponge like nanostructures into the PA layer, a morphological result observed in this study suggests the homogeneous formation of unique highly porous AWC/PA structures with reduced water transport resistance at the interface of the selective layer with the PSf support. Such membranes provided the best performances in terms of water transport

and selectivity, and the porous structure did not affect the mechanical resistance or the membrane properties under RO filtration, unlike previous results reported for PA membranes prepared with additives.[25,28]

It can be concluded that the improved transport performances stem from a combination of higher porosity of the overall PA-based layer, the absence of defects, and the occurring fast transport through the **HC6** nanostructures, whose excellent supramolecular adaptive properties confirm their ability to selectively translocate water while rejecting small ions even when incorporated into hybrid PA-AWC membranes. A significant loss in the perm-selectivity was instead observed for the membranes fabricated with too low MPD concentration or too high **HC6** loadings. For example, membranes fabricated with insufficient MPD exhibited a dense, more symmetric, and extremely thin selective layer. These results suggest that the presence of an excess of MPD seems to be imperatively needed for synthetizing defect-free bioinspired layers.[29]

We know from literature data that the use of a spray coated CNT layer on the PES support before the IP, provides an interface that enables the generation of a highly permeable and selective PA layer with a large effective surface area for water transport.[30] Some similarities may explain the formation mechanism related to this study, whereby the incorporation of **HC6** in the PA layer leads to combined effects, such as the formation of a gutter layer or the generation of higher surface roughness and/or a leaf-like morphology that might be related to the amphiphilic properties of the **HC6** (in contrast to the use of additives, such as SDS). Nonetheless, if we look at the experimental results in the upper bound graph (Fig. 5c), our membranes show to be highly permeable and selective, lying at the limit that exists between BWRO and SWRO regions. High recovery and fouling experiments (See SI Appendix, Figs S8, S9) confirm the high-quality features of our biomimetic membranes. Therefore, in the range/area that delimitates the BWRO membranes, our membranes are highly selective, more selective than the other membranes prepared on laboratory scale, including thin-film nanocomposites (TFN) obtained using nanofillers (i.e., zeolites, carbon nanotubes, graphene oxide), additives (i.e., proton acceptors, surfactants, acids), or optimized by using salts/hydrophilic additives, different solvent or co-solvent, or by varying other experimental conditions (i.e., pH, T or concentrations in the casting solutions) during the membrane fabrication.[11]

Of particular interest is the potential ability of such PA films to present directional pathways for water transport. Herein, microscopy studies revealed that such hybrid PA-AWC materials are composed by AWC crystalline nanoparticles, randomly dispersed in the PA matrix (Fig. 5b). For 1.2-1.8 % w/w MPD these particles are homogeneously and densely distributed within all the thickness of the PA layer, while for lower concentration of 0.2-0.8 % w/w MPD the are less dense and are situated the middle part of the PA layer. For the sponge like nanoparticles[17] of 20-40 nm the permeability of water can be theoretically estimated up to P_{AWC} = 131 $L \cdot m^{-2}\ h^{-1}\ bar^{-1}$ (see SI Appendix). Independently of what is possible by microscopy or not, a high density of channels percolating from one side to the other of the membranes would be ideal, but we are not there yet. It is not about alignment which is clearly proved to occur along nanometric distances of crystals of AWC that are showing order. It is about percolation and high density of channels that for the moment is achieved at this nanometric scale. Although these nanoparticles do not merge to cross the µmetric PA films (Fig. 5a), they are randomly distributed within the PA layer (P_{PA}=1 LMH/bar). The AWC crystals locally contribute to enhance translocation of water, as $P_{AWC} >> P_{PA}$ (Fig. 5b). We do not intent to prove anything in a definite or exactly mathematical way here it is only an intuitive way to explain our results on AWC-PA membrane permeabilities that are experimental and unquestionable. The hybrid PA-AWC materials are reminiscent with previous hybrid ion-channels siloxanes, providing high ionic conduction through their nanometric self-organization of binding sites in hybrid materials.[31-33]

The assumption is that, beside 1. the tunable formation of colloidal nanoparticles within the PA, 2. the formation of inner porosity/voids (as a consequence of the effect of the **HC6** “interlayer”), and

3. the gutter layer-like structure, there is the diffusion of hydrophilic and selective sponge-like AWCs-PA (which we surmise are also in the form of I-quartets). Thus, we assume that this performance is achieved thanks to the combined effect of all these aspects. It is also true that the AWCs are intrinsically “nanofillers” but, by comparison, our membranes are more selective and permeable, possibly due to the compatibility of the **HC6**. Obviously, a high density of channels is desired to promote high permeance. Alignment is not essential, but the percolation of AWC particles is important and should be optimized to have the water transport mainly taking place through the channels. Homogeneous distribution with particle percolation should be preferred. High density of particles without aggregation should be obtained. Achieving these conditions was a main goal of the optimization in this work.

In this work, bioinspired membranes for low salinity BWRO and TWRO water desalination were fabricated by incorporating I-quartet AWC in the classical PA layer. Specifically, the performance of hybrid AWC-PA membranes was tuned by studying the effect of the optimal AWC loads and that of MPD monomer concentration during IP, thus optimizing the selective layer. It may be concluded that self-aggregated AWC colloidal nanoparticles were incorporated by means of their supramolecular interactions with MPD monomer and their presence altered the IP process, and thus the final layer properties. These dynamic self-assembly processes amount to adaptive colloidal entities with the nascent PA oligomers.

This study illustrates a complete interplay of supramolecular aggregation and IP processes:

a) related to supramolecular aggregation, once the AWC load is increasing, the selective PA-AWC layers became more porous and AWC nanoaggregates were homogeneously distributed within the hybrid PA, resulting in high-performance membranes. However, overly high concentrations of AWC nanoaggregates led to the formation of defects, resulting in the poorest performances.

b) The MPD monomer concentration had also an important effect during membrane fabrication and seamless biomimetic layers were synthetized by adjusting this parameter reaching the optimal **HC6**/MPD ratio between 0.7 and 1.9 w/w. In general, a minimum concentration of MPD (~0.8% w/w) was required to obtain high selectivity. However, even this concentration should not be too high in order to maintain high water fluxes. In particular, the membranes fabricated with 1.2 % w/w MPD and 1.5% w/w **HC6** provided a ~360% increase in water permeance at equivalent water to salt flux ratio with respect to the membrane fabricated using 3.4 % w/w MPD.

The best membranes displayed excellent productivity of 110 L m^{-2} h^{-1} under 15.5 bar applied pressure and 35 L m^{-2} h^{-1} under 6 bar applied pressure, while maintaining high selectivity properties, outperforming current BWRO and TWRO commercial membranes. Ultimately, we demonstrated that bioinspired membranes incorporating I-quartet AWCs own the potential for improving existing low-pressure RO applications and their composition can be adjusted to tune their superstructures and performances to target different applications.

Methods Section

Chemicals, Membrane morphological and physio-chemical characterization, Dynamic light scattering (DLS) measurements, Attenuated total reflectance-Fourier transform infrared spectroscopy (ATR-FTIR), Scanning electron microscopy (SEM), Transmission Electronic Microscopy (TEM) and Membrane performance evaluation are presented in supporting information -see SI appendix

Acknowledgments

This work was supported by Agence Nationale de la Recherche ANR-18-CE06-0004-02, WATERCHANNELS and ERANETMED 2-72-357 IDEA.

References

1. T. E. Culp, B. Khara, K. P. Brickey, M. Geitner, T. J. Zimudzi, J. D. Wilbur, St D. Jons, A. Roy, M. Paul, B. Ganapathysubramanian, A. L. Zydney, M. Kumar, E. D. Gomez, *Science*, 371, 72-75 (2021).

2. M. Di Vincenzo, A. Tiraferri, V.-E. Musteata, S. Chisca, R. Sougrat, L.B. Huang, S. P. Nunes, M. Barboiu, Biomimetic artificial water channels membranes for enhanced desalination. *Nature Nanotech. 16*, 190-196 (2020).

3. A. G. Fane, R. Wang, M. X. Hu, Synthetic membranes for water purification: Status and future. *Angew. Chem. Int. Ed.* 54, 3368–3386 (2015).

4. W. J. Lau, S. Gray, T. Matsuura, D. Emadzadeh, J. P. Chen, A. F. Ismail, A review on polyamide thin film nanocomposite (TFN) membranes: History, applications, challenges and approaches. *Water Res.* 80, 306–324 (2015).

5. J. Imbrogno, G. Belfort, Membrane Desalination: Where Are We, and What Can We Learn from Fundamentals? *Annu. Rev. Chem. Biomol. Eng.* 7, 29–64 (2016).

6. L. He, L. F. Dumée, C. Feng, L. Velleman, R. Reis, F. She, W. Gao, L. Kong, Promoted water transport across graphene oxide-poly(amide) thin film composite membranes and their antibacterial activity. *Desalination* 365, 126–135 (2015).

7. H. J. Kim, M. Y. Lim, K. H. Jung, D. G. Kim, J. C. Lee, High-performance reverse osmosis nanocomposite membranes containing the mixture of carbon nanotubes and graphene oxides. *J. Mater. Chem. A* 3, 6798–6809 (2015).

8. M. Safarpour, V. Vatanpour, A. Khataee, H. Zarrabi, P. Gholami, M. E. Yekavalangi, High flux and fouling resistant reverse osmosis membrane modified with plasma treated natural zeolite. *Desalination* 411, 89–100 (2017).

9. W. F. Chan, H. Y. Chen, A. Surapathi, M. G. Taylor, X. Shao, E. Marand, J. K. Johnson, Zwitterion functionalized carbon nanotube/polyamide nanocomposite membranes for water desalination. *ACS Nano* 7, 5308–5319 (2013).

10. M. Di Vincenzo, M. Barboiu, A. Tiraferri, Y. M. Legrand, Polyol-functionalized thin-film composite membranes with improved transport properties and boron removal in reverse osmosis. *J. Memb. Sci.* 540, 71-77 (2017).

11. Z. Yang, H. Guo, C. Y. Tang, The upper bound of thin-film composite (TFC) polyamide membranes for desalination. *J. Memb. Sci.* 590, 117297 (2019).

12. M. Barboiu, A. Gilles, From natural to bio-assisted and biomimetic artificial water channel systems. *Acc. Chem. Res* 46, 2814–2823 (2013).

13. A. Giwa, S. W. Hasan, A. Yousuf, S. Chakraborty, D. J. Johnson, N. Hilal, Biomimetic membranes: A critical review of recent progress. *Desalination* 420, 403–424 (2017).

14. Y. Leduc, M. Michau, A. Gilles, V. Gence, Y. M. Legrand, A. van der Lee, S. Tingry, M. Barboiu, Imidazole-Quartet Water and Proton Dipolar Channels. *Angew. Chem. Int. Ed.* 50, 11366–11372 (2011).

15. M. Barboiu, Artificial water channels *Angew. Chem. Int. Ed.* 51, 11674–11676 (2012).

16. X. B. Hu, Z. Chen, G. Tang, J. L. Hou, Z. T. Li, Single-Molecular Artificial Transmembrane Water Channels. *J. Am. Chem. Soc.* 134, 8384–8387 (2012).

17. S. Murail, T. Vasiliu, A. Neamtu, M. Barboiu, F. Sterpone, M. Baaden, Water permeation across artificial I-quartet membrane channels: from structure to chaos. *Faraday Discuss.* 209, 125–148 (2018).

18. B. Gong, Artificial water channels: Inspiration, progress, and challenges. *Faraday Discuss.* 209, 415–427 (2018).

19. *Artificial Water Channels: Faraday Discuss.* 209 (The Royal Society of Chemistry, 2019).

20. E. Licsandru, I. Kocsis, Y. X. Shen, S. Murail, Y. M. Legrand, A. van der Lee, A. D. Tsai, M. Baaden, M. Kumar, M. Barboiu, Salt-Excluding Artificial Water Channels Exhibiting Enhanced Dipolar Water and Proton Translocation. *J. Am. Chem. Soc* 138, 5403–5409 (2016).

21. I. Kocsis, M. Sorci, H. Vanselous, S. Murail, S. E. Sanders, E. Licsandru, Y. M. Legrand, A. van der Lee, M. Baaden, P. B. Petersen, G. Belfort, M. Barboiu, Oriented chiral water wires in artificial transmembrane channels. *Science Adv.* 4, eaao5603 (2018).

22. V. Freger, Kinetics of film formation by interfacial polycondensation. *Langmuir* 21, 1884–1894 (2005).

23. V. Freger, J. Gilron, S. Belfer, TFC polyamide membranes modified by grafting of hydrophilic polymers: An FT-IR/AFM/TEM study. *J. Memb. Sci.* 209, 283–292 (2002).

24. L. F. Liu, S. C. Yu, Y. Zhou, C. J. Gao, Study on a novel polyamide-urea reverse osmosis composite membrane (ICIC-MPD). I. Preparation and characterization of ICIC-MPD membrane. *J. Memb. Sci.* 281, 88–94 (2006).

25. H.; Yan, X. Miao, J. Xu, G. Pan, Y. Zhang, Y. Shi, M. Guo, Y. Liu, The porous structure of the fully-aromatic polyamide film in reverse osmosis membranes.*J. Memb. Sci.* 475, 504–510 (2015).

26. H. Matsumoto, Y. Konosu, N. Kimura, M. Minagawa, A. Tanioka, Membrane potential across reverse osmosis membranes under pressure gradient. *J. Coll. Interf. Sci.* 309, 272–278 (2007).

27. Y. Mansourpanah, K. Alizadeh, S. S. Madaeni, A. Rahimpour, H. Soltani Afarani, Using different surfactants for changing the properties of poly(piperazineamide) TFC nanofiltration membranes. *Desalination* 271, 169–177 (2011).

28. S. Hermans, R. Bernstein, A. Volodin, I. F. J. Vankelecom, Study of synthesis parameters and active layer morphology of interfacially polymerized polyamide-polysulfone membranes. *React. Funct. Polym.* 86, 199–208 (2015).

29. J. Wei, X. Liu, C. Qiu, R. Wang, C. Y. Tang, Influence of monomer concentrations on the performance of polyamide-based thin film composite forward osmosis membranes. *J. Memb. Sci. 381*, 110–117 (2011).

30. Z. Zhou, Y. Hu, C. Boo, Z. Liu, J. Li, L. Deng, X. An, High-performance thin-film composite membrane with an ultrathin spray-coated carbon nanotube interlayer, *Environ. Sci. Technol. Lett.* 5, 243–248 (2018).

31. M. Barboiu, S. Cerneaux, G. Vaughan, A. van der Lee, Ion-driven ATP-pump by Self-Organized Hybrid Membrane Materials*. J. Am. Chem. Soc.*126*, 3545-3550 (*2004*).*

32. M. Michau, M. Barboiu, Self-organized proton conductive layers in hybrid proton exchange membranes, exhibiting high ionic conductivity. *J. Mater. Chem.* 19, 6124-6131 (2009).

33. M. Barboiu, Constitutional hybrid materials-toward selection of functions. *Eur J. Inorg. Chem.* 1112-1125 (2015).

Figures and Tables

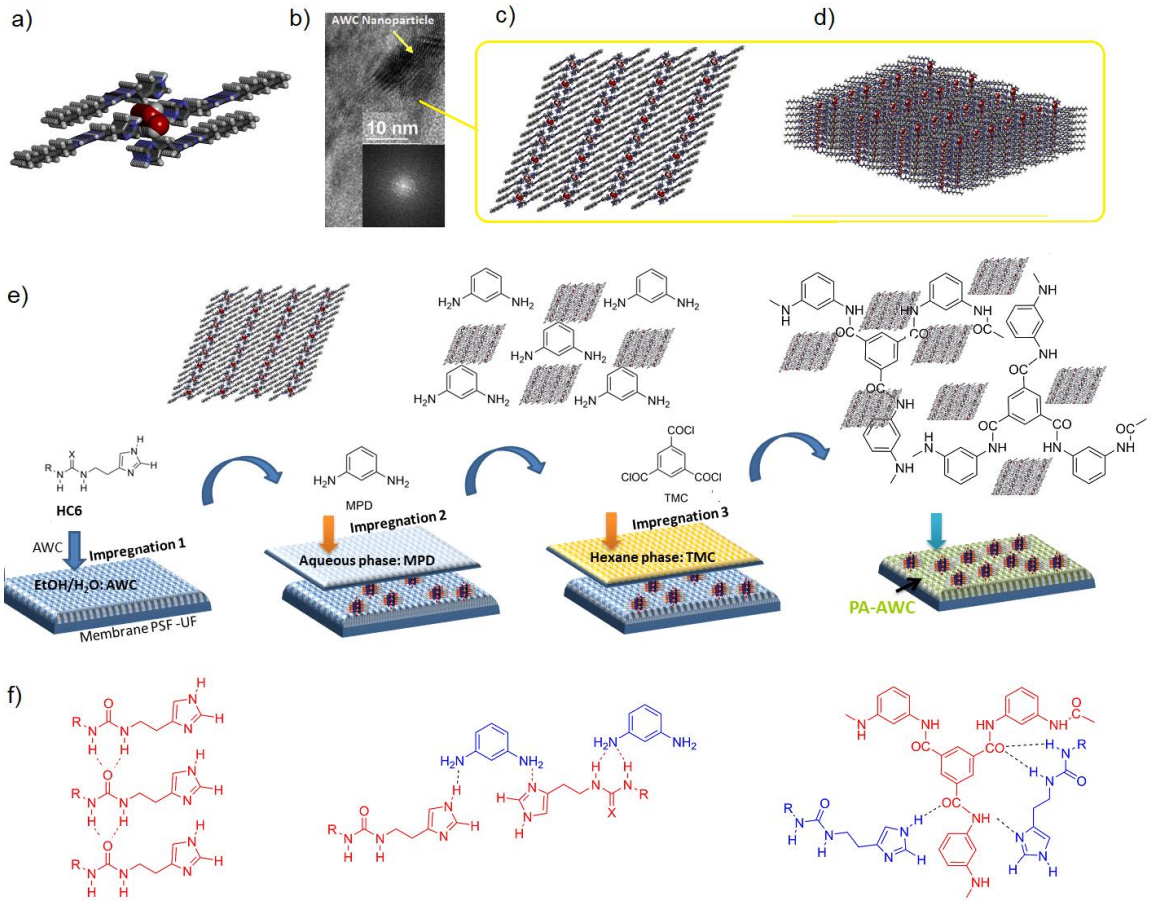

Fig. 1. Membrane synthesis a) I-quartet AWC, b) High TEM magnification of the lamellar crystalline nanoparticles, obtained from the evaporation of an ethanolic/aqueous solution of HC6 and c) top and d) lateral views of single-crystal lamellar packing of I-quartet AWC; e) Synthetic procedure for the hybrid PA/AWC membrane preparation: impregnation 1 of PSf support with a solution of HC6 -formation of colloidal lamellar phases of AWCs, followed by the impregnation 2 with an aqueous solution of m-phenylenediamine (MPD)-interacting *via* f) H-bonding with AWC colloidal particles and by the impregnation 3 with a hexane solution of trimesoylchloride (TMC) resulting in the formation of hybrid H-bonded PA/AWC layers *via* the nucleation/IP processes.

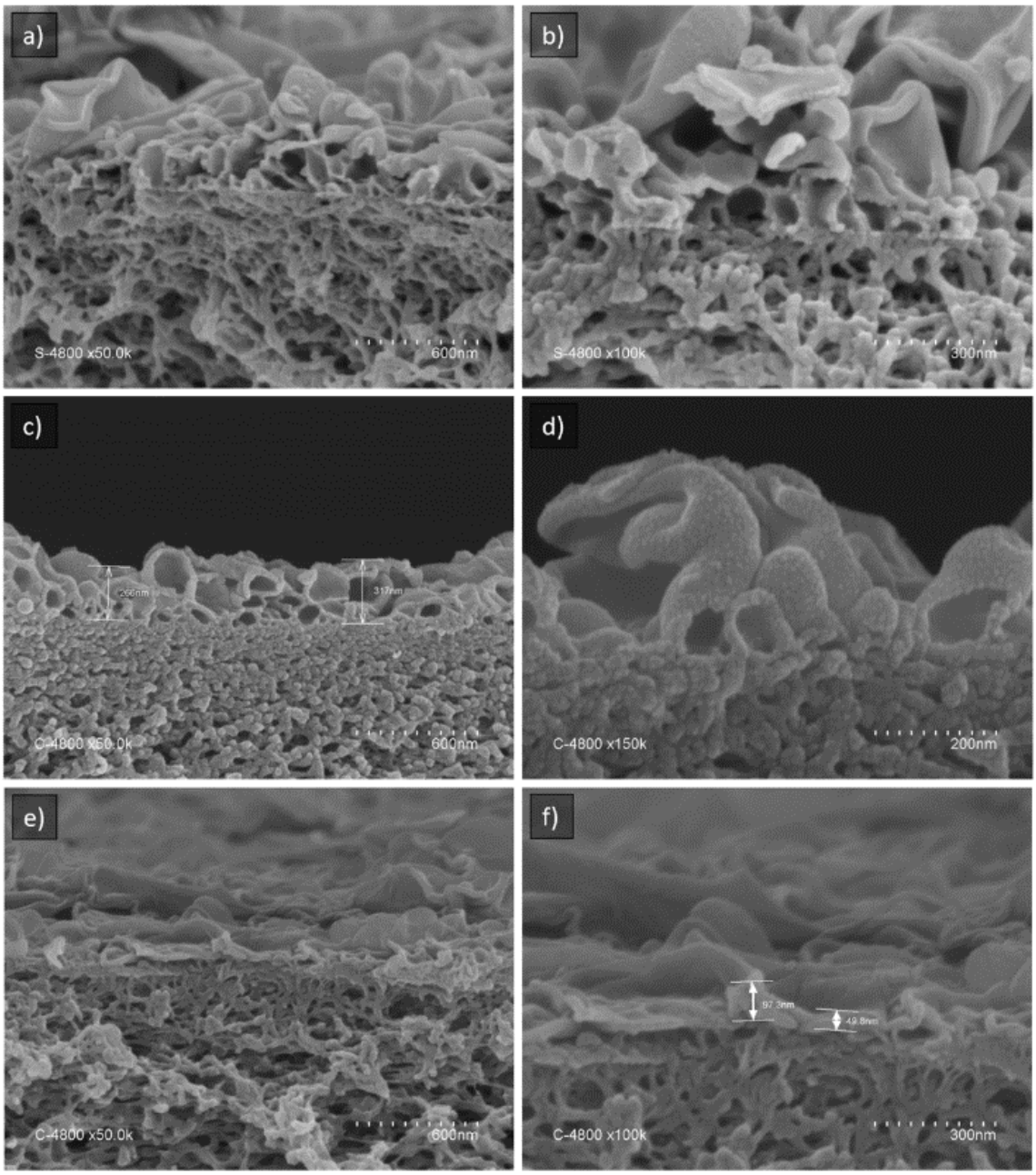

Fig. 2. Representative cross-section SEM micrographs of (a,b) H-0.9; (c,d) 0.8-**HC6** and (e,f) 0.2-**HC6**. MPD concentrations in the casting solutions were (a,b) 3.4%; (c,d) 0.8%; (e,f) 0.2% (w/w). **HC6** concentrations in the casting solutions were (a,b) 0.9%; (c,f) 1.5% (w/w).

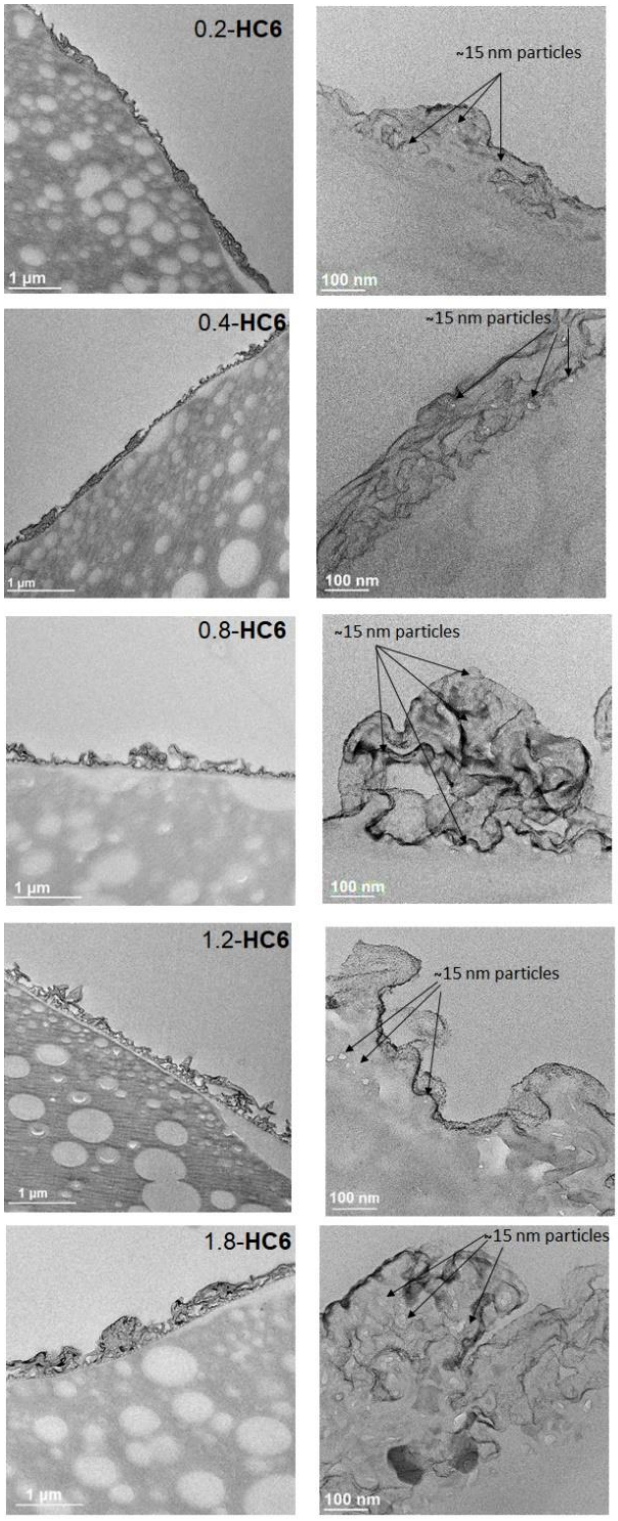

Fig. 3. TEM cross-sectional image of a) 0.2-**HC6**, b) 0.4-**HC6**, c) 0.8-**HC6**, d) 1.2-**HC6**, and e) 1.8-HC6 membranes, % w/w MPD, 0.1 w/w% TMC and 1.5% w/w **HC6** stained with $Zn(NO_3)_2$) showing the detail of the top hybrid layer containing AWC/PA white nanoparticles embedded with high precision in darker PA matrix.

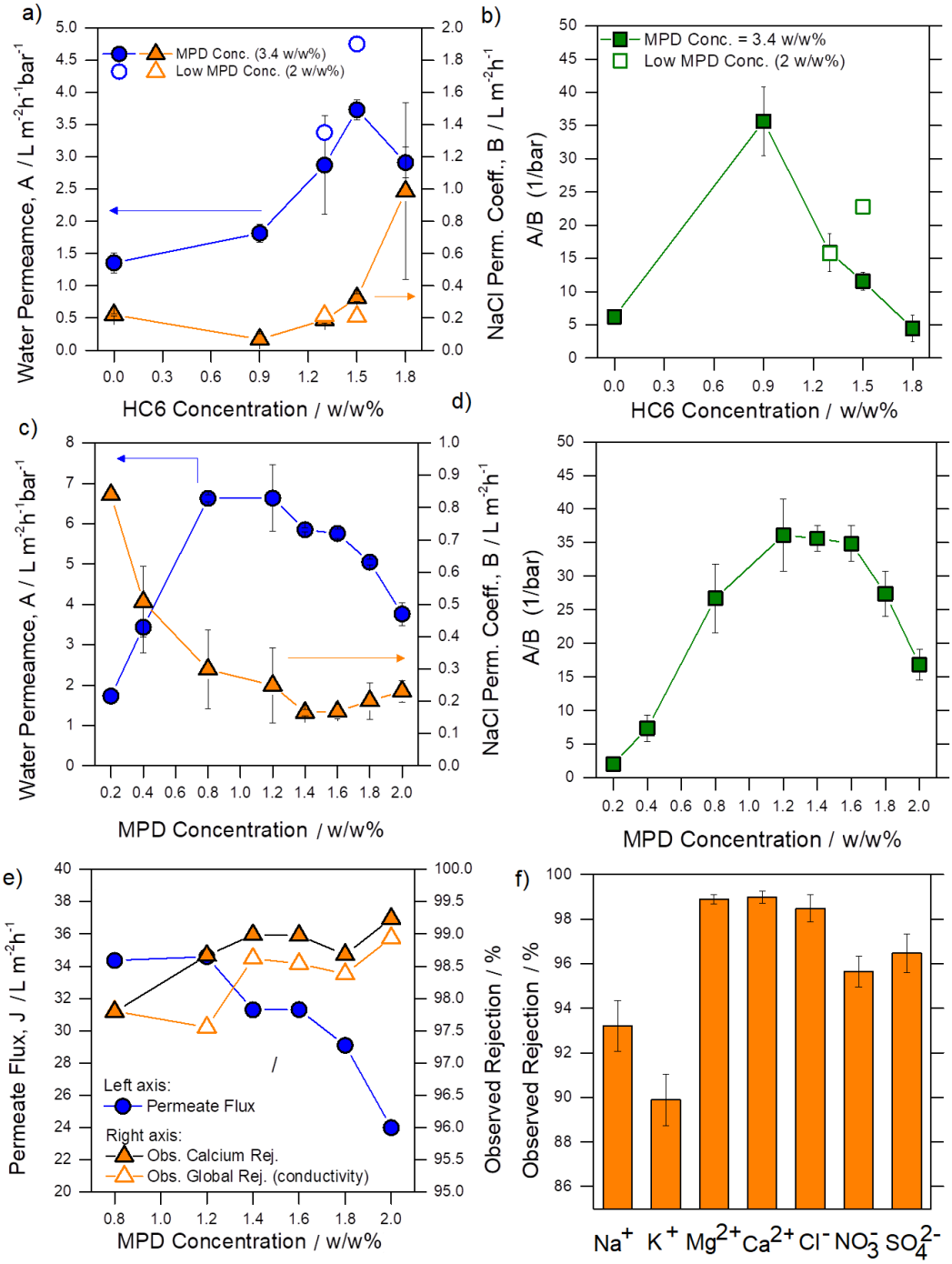

Fig. 4. BWRO desalination performances at 15.5 bar as a function of (a,b) HC6 and (c,d) MPD concentrations. Experimental conditions: pure water for the measurement of *A*; 100 mM NaCl in the feed solution for the measurement of *B*. TWRO desalination performance at 6 bar e) Permeate flux and observed rejection at steady-state as a function of MPD concentration. f) Observed rejection of different cations and anions at steady-state of 1.6-HC6 membranes under TWRO conditions. Lines connecting the data points are only intended as a guide for the eye.

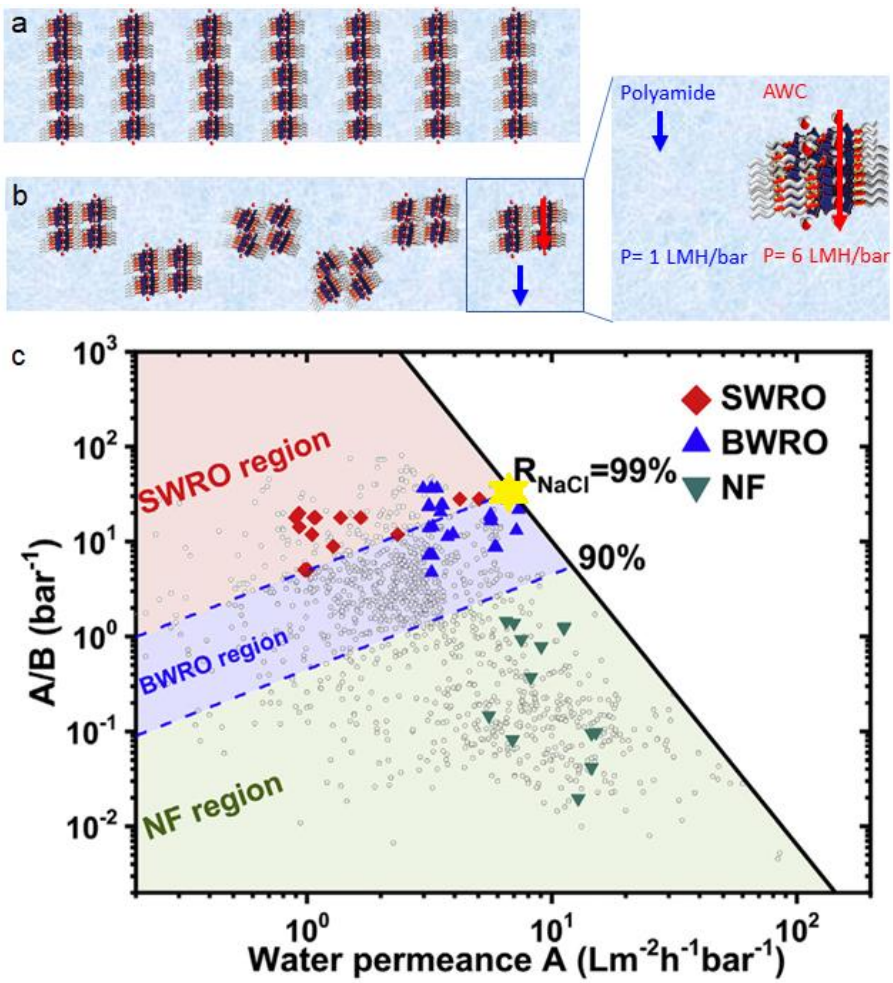

Fig. 5. Enhancement permeation mechanism. a) the ideal membrane with perfectly aligned channels though the whole thickness of the PA membrane (blue); b) uniform aleatory distribution of AWC nanoparticles within the layer. Enhanced permeation at the nanometric level relates to AWCs nanoparticles regions-see text for the details; c) Water permeance and selectivity of commercial seawater reverse osmosis (SWRO, red), brackish water RO (BWRO, blue) and NF membranes (green). Blue dash lines correspond to the NaCl rejection of 99% and 90%, respectively, at a flux of 20 $L \cdot m^{-2} \cdot h^{-1}$. The yellow star highlights the perm-selectivity performance of our optimized BWRO membranes prepared using AWCs, while the empty symbols represent all the other laboratory scaled membranes[11] Fig. adapted from ref. 11 Copyright Elsevier 2019.

PNAS
www.pnas.org

Supplementary Information for

Tuneable bio-inspired membranes incorporating artificial water channels for high-performance brackish/tap water reverse osmosis desalination

Maria Di Vincenzo,[1] Alberto Tiraferri,[2] Mihai Deleanu,[1] Didier Cot,[1] Valentina-Elena Musteata,[3] Stefan Chisca,[3] Suzana P. Nunes,[3] Mihail Barboiu[1]

1Institut Européen des Membranes, Adaptive Supramolecular Nanosystems Group, University of Montpellier, ENSCM, CNRS, Place Eugène Bataillon, CC 047, F-34095, Montpellier, France.
2Department of Environment, Land and Infrastructure Engineering (DIATI), Politecnico di Torino, Corso Duca degli Abruzzi 24, 10129 Turin, Italy.
3King Abdullah University of Science and Technology (KAUST), Biological and Environmental Science and Engineering Division, Advanced Membranes and Porous Materials Center, 23955-6900, Thuwal, Saudi Arabia.

Mihail Barboiu

Email: mihail-dumitru.barboiu@umontpellier.fr

This PDF file includes:

Supplementary text

Fig.s S1 to S7

Tables S1 to S5

METHODS

Chemicals.

Commercial flat-sheet polysulfone (PSf) ultrafiltration membranes, PS35-GPP (Solecta, USA), were used as support layers for the fabrication of all the polyamide-based membranes. Trimesoyl chloride (TMC, 98%), m-phenylenediamine (MPD, flakes 99%), histamine (≥97%), hexyl isocyanate (97%), sodium chloride (NaCl) (≥99.5%), sodium metabisulfite (Na2S2O5, 98%), were purchased from Sigma-Aldrich, France. Artificial water channels precursor HC6 has been synthesized as previously reported.14 All solvents used in this study were HPLC grade. Methanol (MeOH), ethanol (EtOH), tetrahydrofuran (THF), ethyl acetate (EtOAc), dimethylacetamide (DMA), acetonitrile (ACN), and hexane were purchased from VWR International Ltd. Unless specified, all chemicals were dissolved in DI water obtained from a Milli-Q ultrapure water purification system (Millipore, France). All the reagents and solvents were used without any further purification.

Membrane morphological and physio-chemical characterization.

Dynamic light scattering (DLS) measurements were performed using a Malvern Zetasizer with a 173° backscatter measurement angle and a quartz cuvette with a square aperture. The samples were prepared by dissolving the HC6 in ethanol to achieve 0.5, 1 and 2.5% w/w. In order to investigate the formation of AWC colloidal aggregates, different amount of water was added to the HC6/ethanol solution under various conditions. We investigated the formation of AWC colloidal aggregates by dynamic light scattering (DLS). Fig. S1a shows the size distribution of hydrodynamic diameter (Dh) after the addition under vigorous stirring of pure water and 2 w/w% aqueous solution of MPD to 1% **HC6** in ethanol to reach EtOH/H2O and EtOH/H2O+MPD =1/3. The D_h of AWC colloidal aggregates is 200 nm when pure water was added, whereas, when 2 w/w% of an aqueous solution of MPD was added, the Dh is reduced to 70 nm and the size distribution became slightly larger (Fig. S1b). This indicate that **HC6** interacts with the MPD through hydrogen bonding, leading to stabilized AWC colloidal aggregates. When a larger amount of water was added to 1% HC6 in ethanol (to reach EtOH/H2O =1/6), we observed a decrease of the Dh of the AWC colloids from 200 nm to 80 nm, and by adding a larger amount of MPD aqueous solution a further reduction of Dh is observed (from 70 nm to 60 nm). Therefore, we believe that during the IP synthesis, when a large amount of MPD aqueous solution is added, nanometer colloidal AWC is formed at the alcohol/water interface in the polysulfone pores.

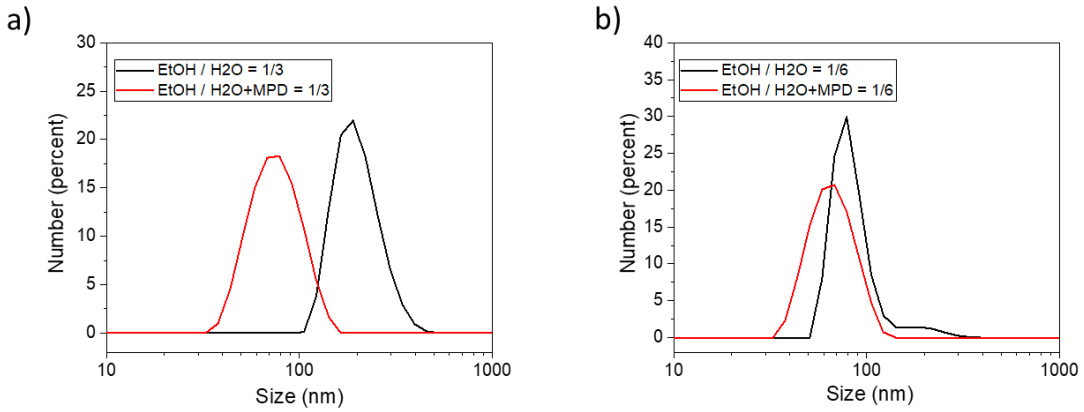

Fig. S1. The size distribution of AWC colloidal aggregates obtained in different conditions by DLS measurements: (**a**) The size distribution of hydrodynamic diameter (D_h) after the addition under vigorous stirring of pure water and 2 w/w% aqueous solution of MPD to 1% HC6 in ethanol to reach EtOH/H_2O = 1/3 and EtOH/H_2O+MPD =1/3; (**b**) The size distribution of D_h after the addition under vigorous stirring of pure water and 2 w/w% aqueous solution of MPD to 1% HC6 in ethanol to reach EtOH/H_2O = 1/6 and EtOH/H_2O+MPD =1/6.

Attenuated total reflectance-Fourier transform infrared spectroscopy (ATR-FTIR) spectra were recorded on a NEXUS spectrometer. The ATR accessory contained a monolithic diamond crystal at a nominal angle of incidence of 45°, yielding 1 internal reflection at the sample surface. All spectra were recorded at 25 °C in the region 625-3500 cm^{-1}. Elemental analysis of the active layers was conducted by energy dispersive X-ray spectroscopy (EDX) using an AZTEC System (Oxford Instruments, UK), at an accelerating voltage of 10 kV and a working distance of 8.5 mm. At least three spectra were captured at different positions to calculate an average atomic percentage of C, N, and O.

Scanning electron microscopy (SEM). The incorporation of HC6 artificial water channels in polyamide layers was verified by a high-resolution scanning electron microscope (SEM, HITACHI S-4800), at an accelerating voltage of 2 kV. For cross-sectional studies, membrane coupons were prepared by freeze-fracturing in liquid nitrogen and then dried in dry air for at least 24 h. A 5-nm thick coating of chromium was sputtered (SC7620 Mini Sputter Coater, Quorum Technologies Ltd.) under Ar atmosphere (10^{-1} mbar) to achieve a minimum conductivity for reliable SEM information. The roughness of the membrane surfaces was investigated by atomic force microscopy (AFM) using a Nanoman, with Nanoscope5 instrument (Bruker Instruments). The tips were from Nanosensors, PPP NCSTR, with a nominal spring constant of 7 N/m and a typical radius of less than 5 nm. All images were acquired in tapping mode with a sampling resolution of at least 512 pts/512 lines using a scan rate of 5.5 Hz for 5 μm^2 areas, and 0.65 Hz for smaller areas.

Transmission Electronic Microscopy (TEM). The membranes were stained by immersion in 1% zinc nitrate aqueous solution for 15 min, followed by rinsing in large amount of distilled water. Zinc salt stained more selectively the imidazole and amide groups in the polyamide layer. Membrane pieces were embedded in epoxy resin (EMbed812, Fisher Scientific), which was thermally cured overnight at 70 °C. Ultrathin sections (100 nm) were cut with an ultramicrotome (Leica EM UC7) and deposited on 200 mesh copper grids. The TEM imaging was performed using a Titan CT microscope (FEI company) operating at 300 kV equipped with a 4k × 4k CCD camera (Gatan, Pleasanton, CA, USA). For HC6 imaging, a drop of solution (1.5 w/w% in ethanol/water 85:15 v/v%) was deposited on carbon coated copper film, blotted with filter paper and let it dry in the lab atmosphere.

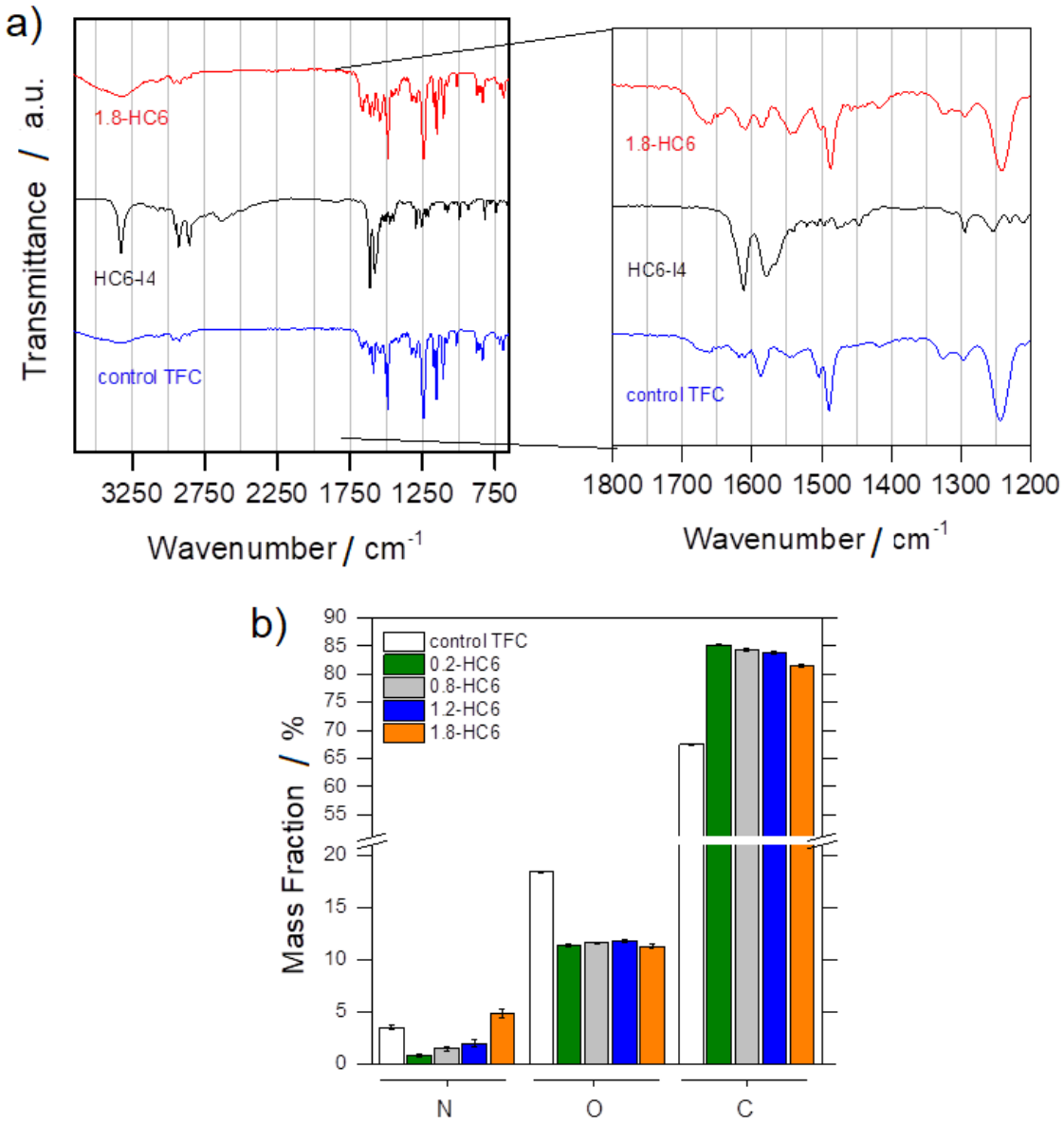

Fig. S2. a) FTIR-ATR spectra of control TFC (blue), HC6 I-quartet (black) and bioinspired membranes (red) (1.8% w/w MPD and 1.5% w/w HC6). b) Atomic mass fraction of % C, N and O from EDX measurements: average values and standard deviations as determined from three different samples for each membrane. The results refer to control TFC membranes (white bar) and to bioinspired membranes (colored bars) containing the optimal concentration of 1.5% w/w HC6, with variable MPD concentrations of 0.2-1.8% w/w.

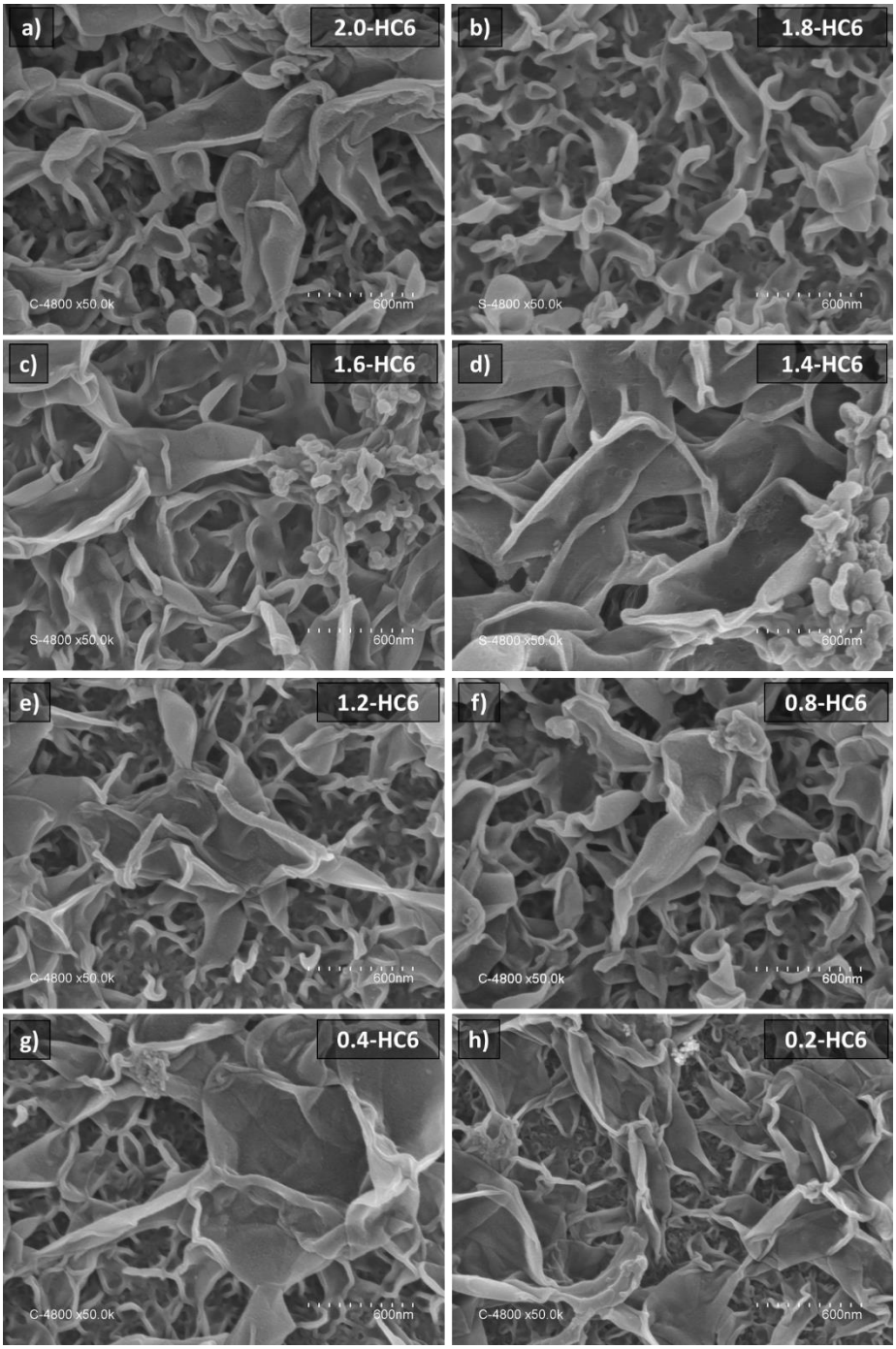

Fig. S3. Representative SEM micrographs of the surface morphology of a) 2.0-HC6; b) 1.8-HC6; c) 1.6-HC6; d) 1.4-HC6; e) 1.2-HC6; f) 0.8-HC6; g) 0.4-HC6; and h) 0.2-HC6 bioinspired membranes prepared with different MPD concentrations during interfacial polymerization (IP). "HC6" stands for optimized precursor concentration (1.5% w/w) and the number before for the actual MPD concentration (% w/w) used during the IP reaction.

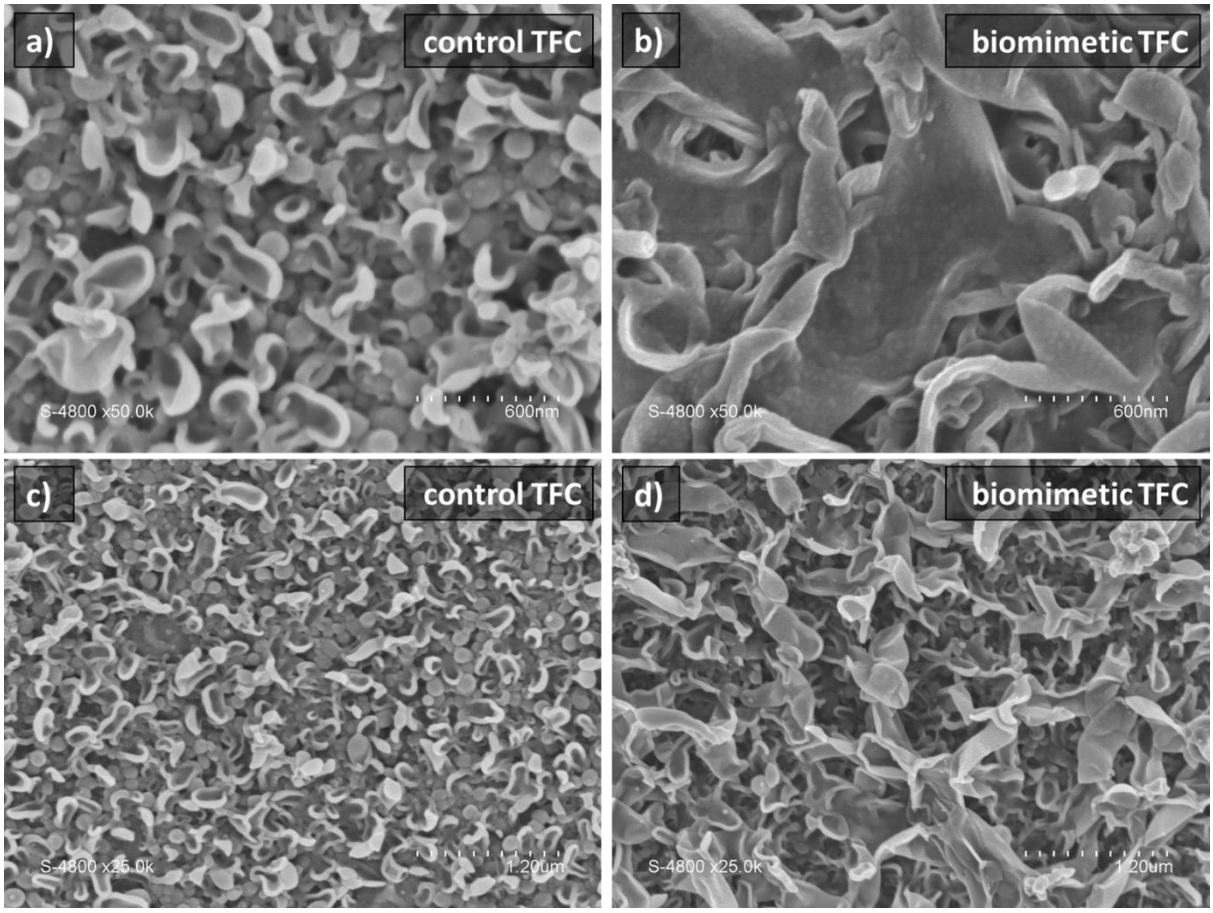

Fig. S4. Representative SEM micrographs of surface top view of, a)-c), control TFC and, b)-d), HC6 bioinspired membrane, showing different morphology and diffused HC6 nanostructures.

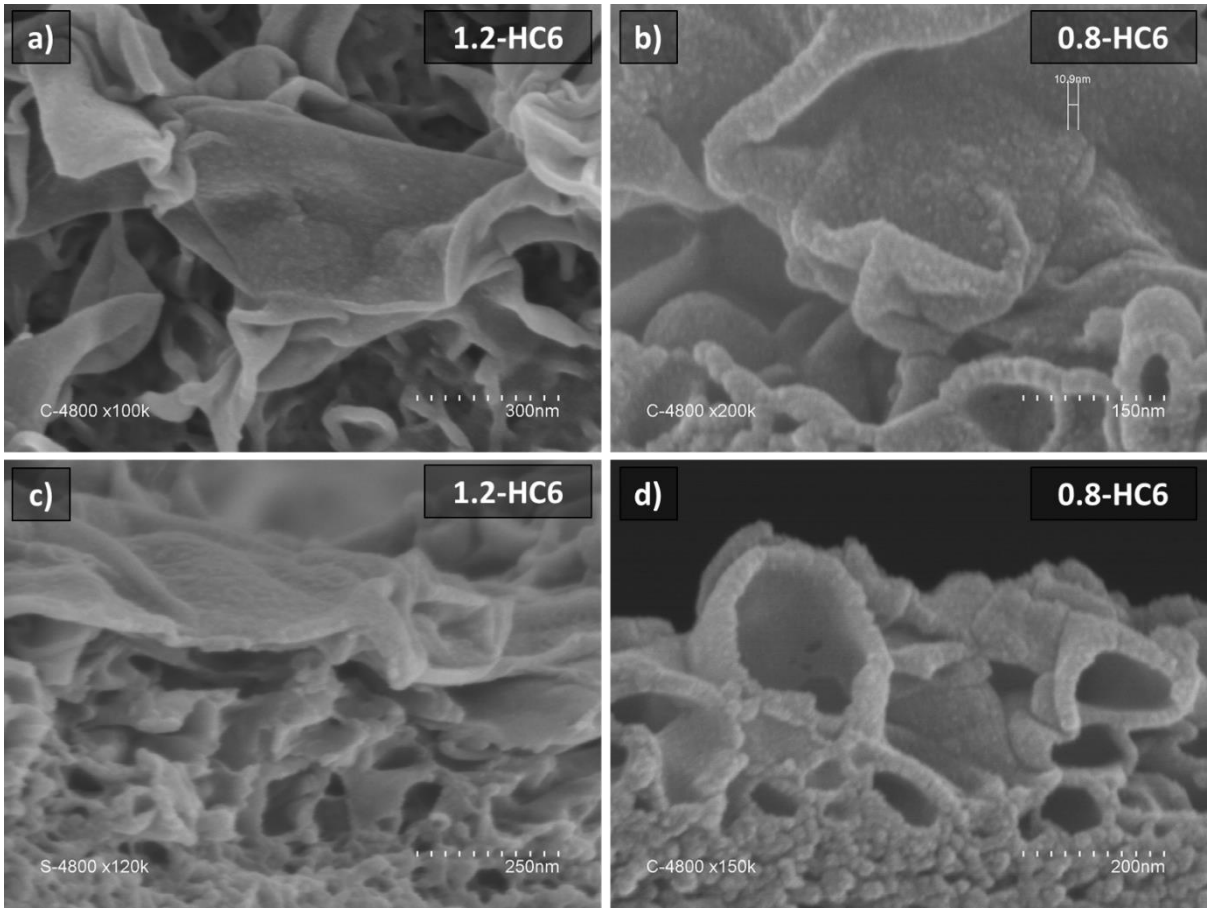

Fig. S5. Representative SEM micrographs of detailed surface top view of a) 1.2-HC6 and b) 0.8-HC6 showing compact HC6 nanostructures. Cross-sectional view of c) 1.2-HC6 and d) 0.8-HC6 showing the detailed distribution of diffused nanoparticles spanning the whole active layers. “HC6” stands for optimized precursor concentration (1.5% w/w) and the number before for the actual MPD concentration (% w/w) used during interfacial polymerization (IP).

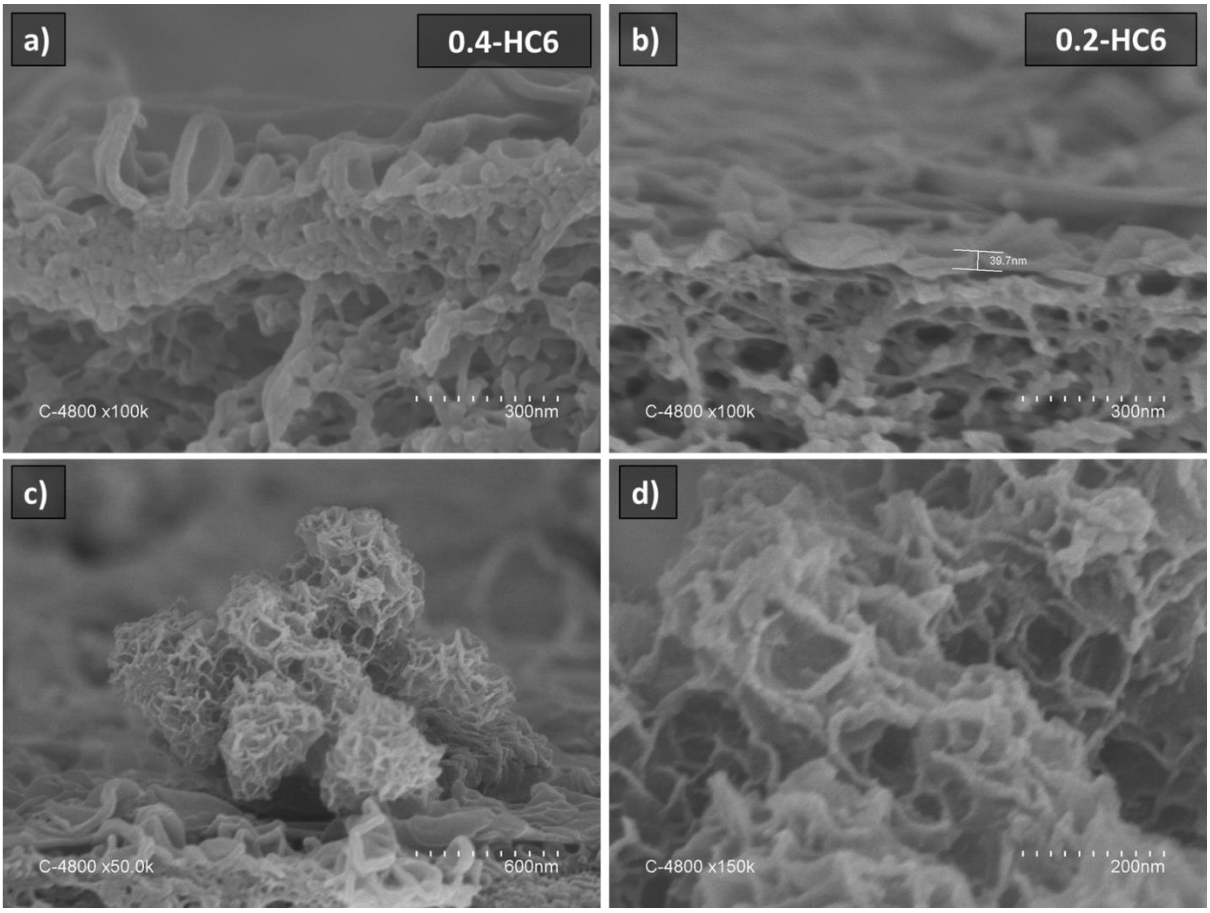

Fig. S6. Representative SEM micrographs of cross-sectional view of a) 0.4-HC6 and b) 0.2-HC6 showing very thin and symmetric dense layers free of inner porosity; “HC6” stands for optimized precursor concentration (1.5% w/w) and the number before for the actual MPD concentration (% w/w) used during the interfacial polymerization reaction. c)-d) Details of nanoaggregates spill from the active layer observed on the surface of biomimetic membranes prepared with substoichiometric MPD concentration, indicating failing in suitable HC6 incorporation.

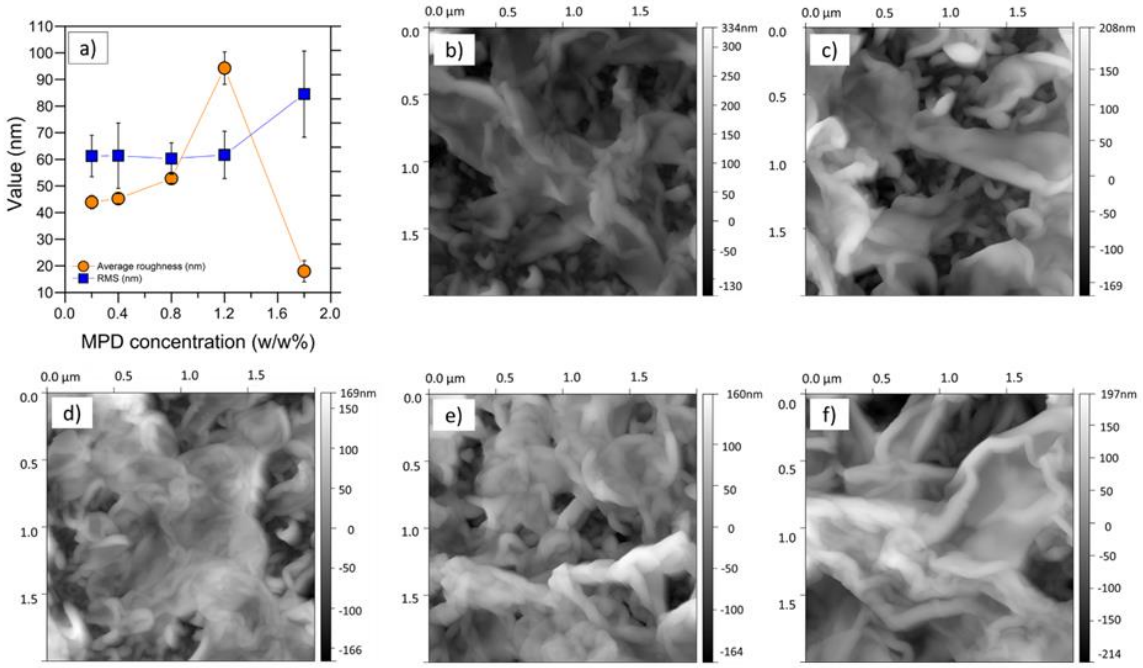

Fig. S7. AFM measurements. a) Experimental and guide to the eye profiles of average and maximum roughness of membranes *versus* MPD concentrations in the casting solutions. The projection area scanned during the measurements was 5 µm × 5 µm. Representative AFM surface images with a projection area of 2 µm × 2 µm of b) 0.2-**HC6**, c) 0.4-**HC6**, d) 0.8-**HC6**, e) 1.2-**HC6**, and f) 1.8-HC6 membranes).

Table S1. Concentrations of **HC6** and MPD in the aqueous phase and TMC in the organic phase for the preparation of different membranes by interfacial polymerization. “H” and “L” stands for high (3.4% w/w) and low (2% w/w) MPD concentration in the aqueous phase

MEMBRANE	HC6	MPD	TMC
	w/w %	w/w %	w/w %
control TFC	-	3.4	0.1
H-0.9	0.9	3.4	0.1
H-1.3	1.3	3.4	0.1
H-1.5	1.5	3.4	0.1
H-1.8	1.8	3.4	0.1
L-1.3	1.3	2.0	0.1
L-1.5	1.5	2.0	0.1
1.8-HC6	1.5	1.8	0.1
1.6-HC6	1.5	1.6	0.1
1.4-HC6	1.5	1.4	0.1
1.2-HC6	1.5	1.2	0.1
0.8-HC6	1.5	0.8	0.1
0.4-HC6	1.5	0.4	0.1
0.2-HC6	1.5	0.2	0.1

Table S2. Energy-dispersive X-ray (EDX) spectroscopy of pristine PA and bioinspired reverse osmosis active layers prepared by varying the MPD monomeric concentration in the casting solutions used during interfacial polymerization (IP). “HC6” stands for optimized precursor concentration (1.5% w/w) and the number before for the actual MPD concentration (% w/w) used during the IP reaction. Atomic mass percentage of C, N, and O were obtained as the average mass fraction value from three different positions of each membrane sample.

Membrane	**C (%)**	**N (%)**	**O (%)**
pristine PA	67.50 ± 0.1	3.50 ± 0.2	18.4 ± 0.10
0.2-HC6	85.15 ± 0.2	0.83 ± 0.1	11.4 ± 0.10
0.8-HC6	84.23 ± 0.2	1.54 ± 0.2	11.6 ± 0.01
1.2-HC6	83.77 ± 0.3	2.01 ± 0.3	11.8 ± 0.08
1.8-HC6	81.47 ± 0.3	4.93 ± 0.4	11.3 ± 0.19

Table S3. Surface roughness parameters of bioinspired reverse osmosis membranes obtained by AFM measurements (projection area of the samples: 5 µm x 5 µm).

Membrane	AVG [nm]	Max [nm]	RMS [nm]
0.2-HC6	44±2	155±45	56±8
0.4-HC6	45±2	200±65	56±13
0.8-HC6	53±2	147±43	55±6
1.2-HC6	95±6	145±90	57±10

Theoretical membrane performance evaluation.

We have calculated the theoretical membrane permeability considering the theoretical values of single permeabilities of single channels and of sponge like structures of HC6 as reported in reference 17. The HC6-I4 single channel permeabilities are 3.8 x 10^6 molecules / s / channel for single channel and 5.25 x 10^7 molecules / s / channel for the sponge-like water channels.[17]

Our results on AWC-PA membrane permeabilities are experimental and unquestionable.
These calculations are performed just to support some discussion as the stability of the channels is clearly different as they a present in bilayer membranes or in crystalline lamellar structures confined within PA matrix. We do not intent to prove anything in a definite or exactly mathematical way here.

We note that the stability of the channels in bilayer is strongly dependent on the size of the tail,[20] while within the crystals the I-quartet pillars are almost similarly stabilized between lamellar hydrophobic phases that are not much altered in the solid state by the dimension of the tail.

Assuming a 3.5 nm thickness (lipid bilayer) and π= 8.3 bar (200 mM NaCl)

HC6-I4 single channel permeability: 3.8×10^6 H_2O / s / channel
From the single crystal structure I4 density: 3.3×10^{17} channels / m^2
The water flux (J_w) is: $J_w = 1.25 \times 10^{24}$ H_2O $m^{-2}s^{-1} = 136.8$ $Lm^{-2}h^{-1}$
Water permeability: $WP = 16.48$ $Lm^{-2}h^{-1}bar^{-1}$

HC6-I4 sponge like channel permeability: 5.25×10^7 H_2O / s / channel
From the single crystal structure I4 density: 3.3×10^{17} channels / m^2
The water flux (J_w) is: $J_w = 1.73 \times 10^{25}$ H_2O $m^{-2}s^{-1} = 1890$ $Lm^{-2}h^{-1}$
Water permeability: $WP = 227$ $Lm^{-2}h^{-1}bar^{-1}$

In the same way we can calculate the water permeation rate **assuming a 20-40 nm thickness *(crystal)* and π= 1.68 bar (34 mM NaCl, same as during the experiments)**

HC6-I4 single channel permeability: 3.8×10^6 H_2O / s / channel
From the single crystal structure I4 density: 3.3×10^{17} channels / m^2
The water flux (J_w) is: $J_w = 1.46 \times 10^{23}$ H_2O $m^{-2}s^{-1} = 15.96$ $Lm^{-2}h^{-1}$
Water permeability: $WP = 9.5$ $Lm^{-2}h^{-1}bar^{-1}$

HC6-I4 sponge like channel permeability: 5.25×10^7 H_2O / s / channel
From the single crystal structure I4 density: 3.3×10^{17} channels / m^2
The water flux (J_w) is: $J_w = 2.02 \times 10^{24}$ H_2O $m^{-2}s^{-1} = 220$ $Lm^{-2}h^{-1}$
Water permeability: $WP = 131$ $Lm^{-2}h^{-1}bar^{-1}$

These values are superior to those observed with conventional BWRO membranes (1-8 $L{\cdot}m^{-2}$ $h^{-1}bar^{-1}$)[11], usually operated at slightly higher 15-18 bars and for higher saline concentrations.

Intrinsic transport properties of control TFC and bioinspired membranes were evaluated using a laboratory-scale cross-flow unit, comprising a high-pressure pump, a feed vessel, and a flat membrane housing cell. The effective membrane active area was 28.9 cm^2, the crossflow velocity was fixed at 0.9 m/s, and the temperature was constant at 25 ± 0.5 °C. Prior to each experiment, the membrane was immersed in water overnight. Two sets of filtration tests were conducted, referred to as “brackish water” and “tap water” tests. The membranes were compacted with DI water as feed at 18 bar (261 psi) of applied pressure, ΔP, until the permeate flux reached a steady-state. The pressure was then lowered to 15.5 bar (217 psi) or 6 bar (87 psi) for brackish water and tap water tests, respectively.

The pure water flux, $J_{w,0}$, was calculated by dividing the volumetric permeate rate, obtained at steady-state, by the membrane active area. The pure water permeability coefficient, A, was determined by dividing the water flux, $J_{w,0}$, by the applied pressure,

$$A = {J_{w,0}}/{\Delta P}.$$

Subsequently, for brackish water tests, NaCl was added from a 5 M stock solution to reach a final concentration of 100 mM, and salt concentrations in the feed and permeate streams were measured using a calibrated conductivity meter (pHenomenal® CO 3100 H, VWR Instruments). The rejection was always measured at steady state (more than one hour after steady state was reached and within this time the selectivity always increased of few decimals). Therefore, the rejection was always constant in time; three separate rejection measurements were performed, distanced 30-60 min from each other In the tap water tests, real tap water was taken from the European Institute of Membranes (IEM) and used as feed stream; salt concentrations were determined by both ion chromatography and conductivity measurements. Upon reaching steady-state, the permeate flux, J_w, was calculated by dividing the volumetric permeate rate by the membrane area. Observed rejection, R, was then computed from the concentrations determined in bulk feed, c_f, and in the permeate stream, c_p, for each ionic species or for global salinity (using conductivity as a proxy for salinity):

$$R = 1 - {c_p}/{c_f}.$$

The rejection values reported for each sample are the average of three different measurements.

The solute permeability coefficient, B, was computed by taking into account the external concentration polarization, as:

$$B = J_w \left(\frac{1-R}{R}\right) e^{\left(-\frac{J_w}{k}\right)},$$

where k is the mass transfer coefficient of the cross-flow cell.

Table S4. TWRO performances of bioinspired active layers; experimental conditions: 6 bar of applied pressure and 25 °C; pure water as feed solution for the measurement of the water permeance *A*; real tap water from the European Institute of Membranes (IEM) for the measurement of the permeate flux with complex real solution; conductivity measurements for the evaluation of the observed global rejection; ionic chromatography measurements for the estimation of the bivalent Ca^{+2} rejection. "**HC6**" stands for optimized precursor concentration (1.5% w/w) and the number before for the actual MPD concentration (% w/w) used during the interfacial polymerization.

Membrane	**A**	**Water Flux**	**Salt Rejection** Conductivity measurements	**Ca^{+2} Rejection** Ionic chromatography
Type	LMH/bar	LMH	%	%
2.0-HC6	3.90	24.0	98.94	99.2
1.8-HC6	4.90	29.1	98.38	98.7
1.6-HC6	5.60	31.3	97.54	98.0
1.4-HC6	5.70	31.3	98.62	99.0
1.2-HC6	6.50	34.6	97.60	98.7
0.8-HC6	6.60	35.1	97.70	97.9

Table S5. Ionic chromatography measurements of ionic concentrations (ppm) of both feed and permeate samples to evaluate the specific ionic separation performances of bioinspired active layers for TWRO desalination. Real tap water was taken from the European Institute of Membranes (IEM) and used as feed stream. The membranes presented in this study were selected because of their higher water flux obtained at an applied pressure of 6 bar, values that are comparable or slightly higher compared to marketed state-of-the-art tap water reverse osmosis membranes, such as TW30 (DuPont). "**HC6**" stands for optimized precursor concentration (1.5% w/w) and the number before for the actual MPD concentration (% w/w) used during the interfacial polymerization.

Ionic Chromatography - Concentrations feed and permeate (ppm) - Real Tap Water									
Membrane	**Sodium**	**Potassium**	**Magnesium**	**Calcium**	**Chloride**	**Chlorate**	**Sulfate**	**Bicarbonate**	**Sample**
Type	**ppm**	**ppm**	**ppm**	**ppm**	**ppm**	**ppm**	**ppm**	**ppm**	**-**
0.8-HC6 (1)	275.22	0.32	1.56	26.17	264.59	2.68	18.43	339	Feed
	5.46	0.07	-	0.51	4.07	0.08	0.84	8	Permeate
0.8-HC6 (2)	172.02	0.41	1.91	29.99	79.95	3.2	20.91	393	Feed
	6.56	0.2	-	0.65	3.32	0.09	0.94	13	Permeate
0.8-HC6 (3)	185.56	0.36	1.76	29.25	98.57	3.12	21.23	394.00	Feed
	5.39	0.07	-	0.73	2.08	0.10	0.90	12	Permeate
1.2-HC6 (1)	137.53	1.19	7.98	91.98	209.39	2.18	19.31	301	Feed
	4.93	0.05	0.08	1.05	3.78	0.08	0.89	9	Permeate
1.2-HC6 (2)	248.05	1.08	9.47	116.72	418.88	2.81	19.35	316	Feed
	9.16	0.1	0.13	1.78	11.11	0.12	0.94	10	Permeate
1.4-HC6 (1)	54.45	1.35	16.91	211.76	274.78	-	24.37	367	Feed
	3.91	0.15	0.23	2.78	6.02	-	0.91	9	Permeate
1.4-HC6 (2)	54.45	1.35	16.91	211.76	274.78	-	24.37	367	Feed
	3	0.14	0.16	1.94	2.72	-	1.04	9	Permeate
1.4-HC6 (3)	28.71	2.03	8.81	128.58	64.26	-	3.50	394	Feed
	2.21	0.18	0.09	1.04	0.90	-	0.09	8	Permeate

Table S6. Ionic chromatography measurements to evaluate the specific ionic rejection performances of bioinspired active layers for TWRO desalination. Real tap water was taken from the European Institute of Membranes (IEM) and used as feed stream. The membranes presented in this study were selected because of their higher water flux obtained at an applied pressure of 6 bar, values that are comparable or slightly higher compared to marketed state-of-the-art tap water reverse osmosis membranes, such as TW30 (DuPont). "**HC6**" stands for optimized precursor concentration (1.5% w/w) and the number before for the actual MPD concentration (% w/w) used during the interfacial polymerization.

Ionic Chromatography - Rejection Average and Standard Deviation – TWRO, ΔP = 6 bar								
Membrane Type	**Sodium %**	**Potassium %**	**Magnesium %**	**Calcium %**	**Chloride %**	**Chlorate %**	**Sulfate %**	**Bicarbonate %**
1.4-HC6	93.20 ± 1.14	89.88 ± 1.14	98.89 ± 0.22	98.99 ± 0.26	98.47 ± 0.61	-	96.48 ± 0.87	97.76 ± 0.18
1.2-HC6	96.36 ± 0.08	93.27 ± 3.58	98.81 ± 0.26	98.67 ± 0.27	97.77 ± 0.60	96.03 ± 0.42	95.27 ± 0.18	96.92 ± 0.12
0.8-HC6	97.10 ± 0.91	79.34 ± 1.72	99.50 ± 0.23	97.80 ± 0.28	97.40 ± 1.37	97.00 ± 0.20	95.57 ± 0.17	97.10 ± 0.49

Protocol for high-recovery experiment

The membranes were compacted at 17 bar until steady-state flux was measured. The pressure was lowered to 15.5 bar and NaCl was added into the feed solution to reach a concentration of 34 mM (2 g/L). The system was thus opened (the permeate stream was not recirculated into the feed tank but collected separately), and the flux constantly monitored until a recovery rate of 75% was obtained. The observed rejection was determined by measuring the conductivity of the feed and the permeate streams throughout the test.

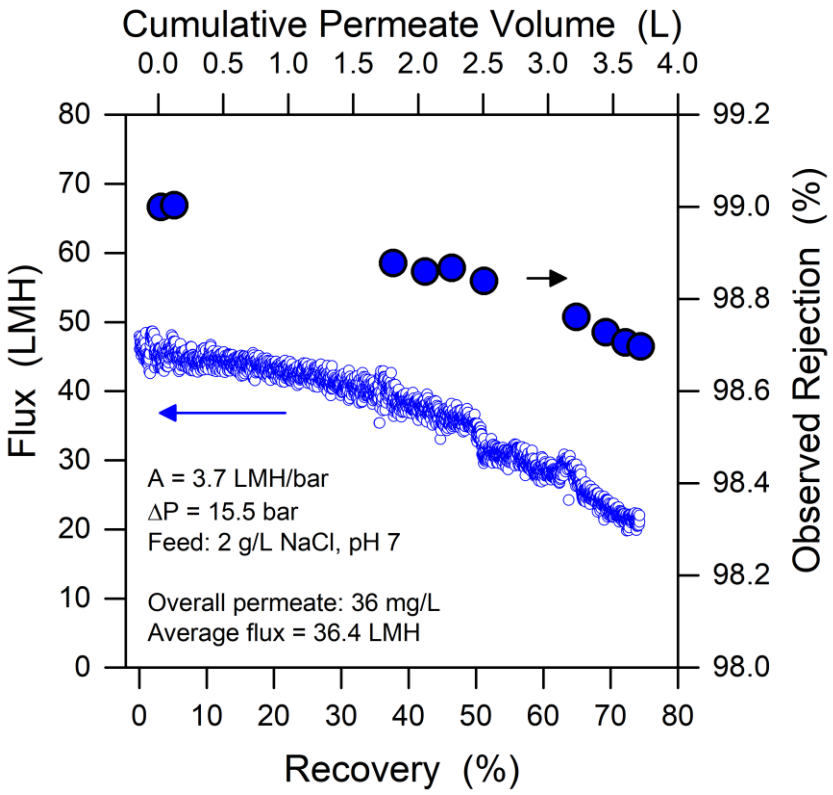

Figure S8. High-recovery filtration experiment, showing (open circles, left axis) the measured flux and (solid circles, right axis) the measured observed rejection as a function of recovery rate. The test was conducted at an applied pressure of 15.5 bar, and feed solutions with the following composition: 34 mM NaCl, pH 7 ± 0.4 (0.1 mM $NaHCO_3$). The crossflow velocity was set at 0.3 m/s, and the temperature was constant at 25 ± 0.5 °C. At 75% recovery, the total permeate had a concentration of 36 mg/L (equivalent to an overall system rejection of 98.2%). The average flux at the end of the test was 36.4 LMH.

Protocol for fouling experiment

The membranes were compacted at 17 bar until steady-state flux was measured. The pressure was lowered to 15.5 bar and NaCl was added into the feed solution to reach a concentration of 34 mM (2 g/L). At steady-state and in closed-loop mode (the permeate stream recirculated into the feed tank), the observed rejection was determined by measuring the conductivity of the feed and the permeate streams three times at intervals of roughly 30 min between each sampling, resulting in values of 99.20 ± 0.04 % and 98.07 ± 0.02 % for the biomimetic membrane and the XLE membrane, respectively. Subsequently, $CaCl_2$, alginate, and BSA were added into the feed solution and the applied pressure was adjusted for each membrane to obtain an initial flux of 42 ± 2 L $m^{-2}h^{-1}$ and to initiate the accelerated fouling test, which was carried out for approximately 18 h.

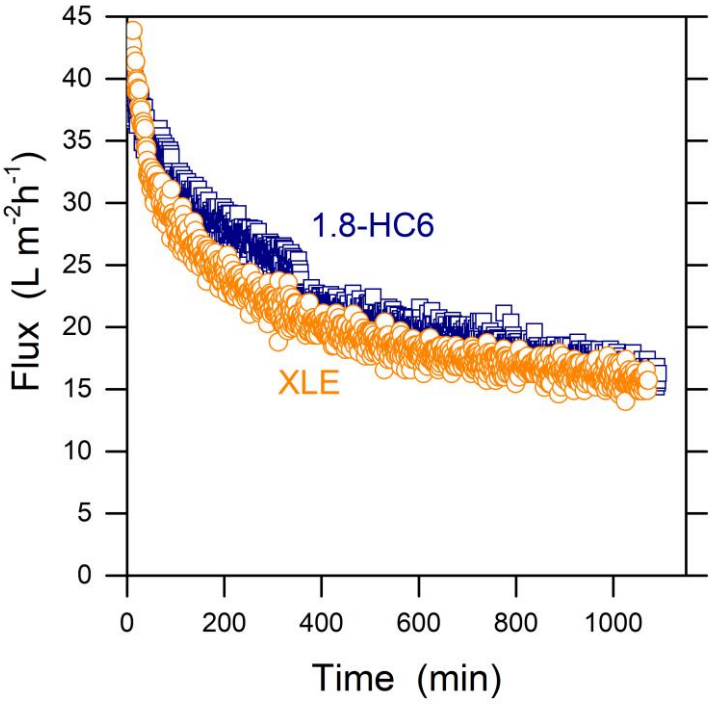

Figure S9. Flux decline due to organic fouling measured with (orange circles) XLE, a commercial brackish water desalination membrane, and with (blue squares) biomimetic 1.8-HC6. The fouling tests were conducted with an initial flux of 42 ± 2 L $m^{-2}h^{-1}$, and feed solutions with the following composition: 34 mM NaCl, 2 mM $CaCl_2$, 50 mg/L alginate, 100 mg/L bovine serum albumin, pH 7 ± 0.4 (0.1 mM $NaHCO_3$). The crossflow velocity was set at 0.3 m/s, and the temperature was constant at 25 ± 0.5 °C. The applied pressure was 15.5 bar for the biomimetic membrane and 11 bar for the commercial XLE membrane.